Fully decoupled time-marching schemes for incompressible fluid/thin-walled structure interaction

Miguel Angel Fernández, Mikel Landajuela

Fully decoupled time-marching schemes for incompressible fluid/thin-walled structure interaction

Miguel A. Fernández, Mikel Landajuela

RESEARCH REPORT
N° 8425
December 2013
Project-Team Reo

ISSN 0249-6399 ISRN INRIA/RR--8425--FR+ENG

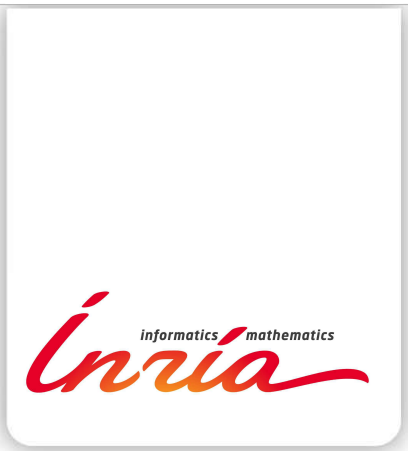

Fully decoupled time-marching schemes for incompressible fluid/thin-walled structure interaction

Miguel A. Fernández *†, Mikel Landajuela*

Project-Team Reo

Research Report n° 8425 — December 2013 — 24 pages

Abstract: In this paper we introduce a class of fully decoupled time-marching schemes (velocity-pressure-displacement splitting) for the coupling of an incompressible fluid with a thin-walled viscoelastic structure. The time splitting combines an overall fractional-step time-marching of the system with a specific Robin-Neumann treatment of the interface coupling. The resulting solution procedures are genuinely partitioned. A priori energy estimates guaranteeing unconditional stability are established for the variants without extrapolation and with first-order extrapolation. The accuracy and performance of the methods proposed are discussed in several numerical examples.

Key-words: fluid-structure interaction, incompressible fluid, Reissner-Mindlin shell, time-discretization, fractional-step method, loosely coupled scheme

This work was supported by the French National Research Agency (ANR) through the EXIFSI project (ANR-12-JS01-0004).

* Inria, REO project-team, Rocquencourt - B.P. 105, F–78153 Le Chesnay cedex, France
† UPMC Université Paris VI, REO project-team, UMR 7958 LJLL, F–75005 Paris, France

RESEARCH CENTRE
PARIS – ROCQUENCOURT

Domaine de Voluceau, - Rocquencourt
B.P. 105 - 78153 Le Chesnay Cedex

Schémas de couplage totalement découplés pour l'interaction d'un fluide incompressible et une structure mince

Résumé : Dans cet article, nous introduisons une classe de schémas entièrement découplés (vitesse-pression-déplacement) pour le couplage d'un fluide incompressible avec une structure viscoélastique mince. Les méthodes combinent une discrétisation à pas fractionnaire globale du système couplé avec un traitement spécifique Robin-Neumann du couplage à l'interface. Des estimations d'énergie a priori garantissent la stabilité inconditionnelle des variantes sans extrapolation et avec extrapolation d'ordre un. La précision et la robustesse des méthodes proposées sont illustrées dans plusieurs exemples numériques.

Mots-clés : interaction fluide-structure, fluide incompressible, modèle de coque Reissner-Mindlin, discrétisation en temps, méthode à pas fractionnaire, schéma de couplage fable

1 Introduction

Mathematical problems describing the coupling of a deformable thin-walled structure with an incompressible fluid flow appear in a wide variety of engineering fields: from sailing boats and parachutes, to heat exchanger tubes, sloshing dynamics in tanks and the biomechanics of blood and airflow (see, e.g., [29, 36, 33, 11, 31, 26]).

The numerical approximation of this type of problems is extremely sensitive to the way the interface coupling conditions (kinematic and kinetic continuity) are treated at the discrete level. This is due, in particular, to the fact that the coupling is very stiff. So called explicit coupling (or *loosely coupled*) schemes, that only involve the solution of the fluid and of the structure once per time-step, are known to be unconditionally unstable for standard Dirichlet-Neumann strategies whenever the amount of added-mass in the system is large (see, e.g., [7]). This explains the tremendous research effort devoted, over the last decade, to the design of robust methods based on alternative coupling paradigms (see, e.g., [12] for a recent review).

Fractional-step methods have played a major role in this attempt (see, e.g., [15, 16, 34, 3, 1, 2, 24, 13, 18, 14, 19, 5, 30]). In these approaches, added-mass free stability is achieved by combining a fractional-step time-marching in the fluid (see, e.g., [16, 34, 3, 1, 2]) or in the solid (see, e.g., [24, 13, 14, 19, 5, 30]) with a specific explicit/implicit treatment of the interface conditions. The implicit part of the coupling guarantees stability while the explicit one reduces computational complexity.

Different degrees of fluid-solid splitting are hence obtained. In the semi-implicit schemes reported in [16, 34, 3, 1, 2] the fluid pressure and the solid system are fully coupled. In [24, 13, 5, 30] the implicit part couples the fluid and hydrodynamic contributions (inertial and viscous effects) of the thin-solid. Full fluid-solid splitting (i.e., explicit coupling) is achieved with the incremental displacement-velocity correction methods introduced [14, 19], which only treat implicitly the solid inertia within the fluid. In short, these methods are Robin-Neumann explicit coupling schemes which introduce optimally consistent perturbations of the interface kinematic constraint, through appropriate semi-implicit treatments of the underlying Robin consistency on the interface.

In this work, we introduce a new class of methods for the coupling of an incompressible fluid with a general thin-walled structure. These schemes enable (for the first time) a fully decoupled time-marching of the entire fluid-solid state, namely, fluid velocity, fluid pressure and solid displacement. The methods combine a Chorin-Temam time-stepping in the fluid with a particular fractional-step time discretization of the interface Robin consistency.

For a representative linear setting, involving a Stokesian fluid and a viscoelastic Reissner-Mindlin shell model, a priori energy estimates are derived for some of the variants, guaranteeing (added-mass free) stability. Several numerical experiments, based on different linear and non-linear fluid-structure interaction examples from the literature, illustrate the accuracy and performance of the methods proposed.

The rest of the paper is organized as follows. In Section 2, we introduces the general fluid-structure coupled problem. Section 3, presents the fully decoupled schemes within a time semi-discrete framework. Section 4 is devoted to the derivation and analysis of the schemes within a representative linear setting. We also discuss there their interpretation as the result of applying an overall fractional-step time-marching on the entire system. The numerical experiments are reported in Section 5. Finally, Section 6 draws the conclusions and a few lines for further investigation.

Some preliminary results of this work have been announced, without proof, in [17].

2 Problem setting

In this section we present the non-linear coupled problem that describes the mechanical interaction between a viscous incompressible fluid and an a thin-walled viscoelastic structure. The fluid is modeled by the incompressible Navier-Stokes equations in ALE (arbitrary Lagrangian-Eulerian) formulation (see, e.g. [21, 10]). The structure is described by a *Reissner-Mindlin* shell model, commonly used in engineering practice (see, e.g., [8, 4]).

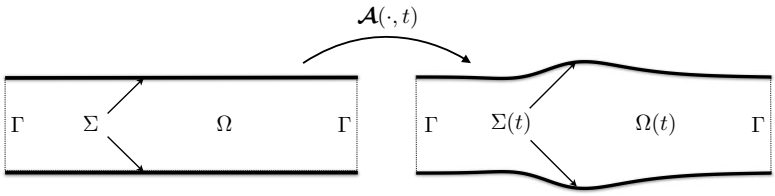

Figure 1: Geometrical description

Let $\Omega \subset \mathbb{R}^3$ be the reference configuration of the fluid domain and denote $\partial\Omega$ its boundary. We consider the following partition $\partial\Omega = \Gamma \cup \Sigma$, where Σ stands for the fluid-structure interface (see Figure 1). Since the structure is thin-walled, the interface Σ is itself the reference configuration of the shell mid-surface. The current configuration of the fluid domain, $\Omega(t)$, is parametrized by the ALE map $\boldsymbol{\mathcal{A}} \overset{\text{def}}{=} \boldsymbol{I}_\Omega + \boldsymbol{d}^{\text{f}}$ as $\Omega(t) = \boldsymbol{\mathcal{A}}(\Omega, t)$, where $\boldsymbol{d}^{\text{f}} : \Omega \times \mathbb{R}^+ \to \mathbb{R}^3$ stands for the displacement of the fluid domain. In the following, the operator $\partial_t|_{\boldsymbol{\mathcal{A}}}$ represents the ALE time derivative, $\boldsymbol{w} \overset{\text{def}}{=} \partial_t \boldsymbol{\mathcal{A}} = \partial_t \boldsymbol{d}^{\text{f}}$ the fluid domain velocity, $\boldsymbol{F} \overset{\text{def}}{=} \boldsymbol{\nabla}\boldsymbol{\mathcal{A}}$ the fluid domain gradient of deformation and $J \overset{\text{def}}{=} \det \boldsymbol{F}$ its Jacobian. The exterior unit-vector normal to $\partial\Omega$ is denoted by $\boldsymbol{n}$ and the symbols $\boldsymbol{v}_\perp \overset{\text{def}}{=} (\boldsymbol{v}\cdot\boldsymbol{n})\boldsymbol{n}$ and $\boldsymbol{v}_{\|} \overset{\text{def}}{=} \boldsymbol{v} - \boldsymbol{v}_\perp$ stand, respectively, for the normal and tangential components of a given vector field $\boldsymbol{v}$ defined on the surface Σ.

The non-linear fluid-structure problem under consideration reads as follows: find the fluid domain displacement $\boldsymbol{d}^{\text{f}} : \Omega \times \mathbb{R}^+ \to \mathbb{R}^3$, the fluid velocity $\boldsymbol{u} : \Omega \times \mathbb{R}^+ \to \mathbb{R}^3$, the pressure $p : \Omega \times \mathbb{R}^+ \to \mathbb{R}$, the solid mid-surface displacement $\boldsymbol{d} : \Sigma \times \mathbb{R}^+ \to \mathbb{R}^3$ and the rotation vector $\boldsymbol{\theta} : \Sigma \times \mathbb{R}^+ \to \mathbb{R}^3$ (satisfying the *Reissner-Mindlin* kinematical assumption, viz., $\boldsymbol{\theta}_\perp = \boldsymbol{0}$) such that

$$
\begin{cases}
\boldsymbol{d}^{\text{f}} = \text{Ext}(\boldsymbol{d}|_\Sigma), \quad \boldsymbol{w} = \partial_t \boldsymbol{d}^{\text{f}} & \text{in} \quad \Omega, \\
\rho^{\text{f}} \partial_t|_{\boldsymbol{\mathcal{A}}} \boldsymbol{u} + \rho^{\text{f}} (\boldsymbol{u} - \boldsymbol{w}) \cdot \boldsymbol{\nabla}\boldsymbol{u} - \mathbf{div}\boldsymbol{\sigma}(\boldsymbol{u}, p) = \boldsymbol{0} & \text{in} \quad \Omega(t), \\
\text{div}\boldsymbol{u} = 0 & \text{in} \quad \Omega(t), \\
\boldsymbol{\sigma}(\boldsymbol{u}, p)\boldsymbol{n} = -p_\Gamma \boldsymbol{n} & \text{on} \quad \Gamma,
\end{cases}
\tag{1}
$$

$$
\begin{cases}
\boldsymbol{u} = \dot{\boldsymbol{d}} & \text{on} \quad \Sigma, \\
\rho^{\text{s}} \epsilon \partial_t \dot{\boldsymbol{d}} + \boldsymbol{L}^{\text{e}}_{\boldsymbol{d}}(\boldsymbol{d}, \boldsymbol{\theta}) + \boldsymbol{L}^{\text{v}}_{\dot{\boldsymbol{d}}}(\dot{\boldsymbol{d}}, \dot{\boldsymbol{\theta}}) = -J\boldsymbol{\sigma}(\boldsymbol{u}, p)(\boldsymbol{F})^{-\text{T}}\boldsymbol{n} & \text{on} \quad \Sigma, \\
\boldsymbol{L}^{\text{e}}_{\boldsymbol{\theta}}(\boldsymbol{d}, \boldsymbol{\theta}) + \boldsymbol{L}^{\text{v}}_{\dot{\boldsymbol{\theta}}}(\dot{\boldsymbol{d}}, \dot{\boldsymbol{\theta}}) = \boldsymbol{0} & \text{on} \quad \Sigma, \\
\dot{\boldsymbol{d}} = \partial_t \boldsymbol{d}, \quad \dot{\boldsymbol{\theta}} = \partial_t \boldsymbol{\theta} & \text{on} \quad \Sigma, \\
\boldsymbol{d} = \boldsymbol{\theta} = \boldsymbol{0} & \text{on} \quad \partial\Sigma,
\end{cases}
\tag{2}
$$

and complemented with the initial conditions $\boldsymbol{u}(0) = \boldsymbol{u}_0$, $\boldsymbol{d}(0) = \boldsymbol{d}_0$ and $\dot{\boldsymbol{d}}(0) = \dot{\boldsymbol{d}}_0$. The symbol $\text{Ext}(\cdot)$ denotes any reasonable lifting operator from the (reference) interface Σ into the reference fluid domain Ω. The constants ρ^{f} and ρ^{s} stand for the fluid and solid densities respectively while

ϵ represents the solid thickness. We assume the fluid to be incompressible and Newtonian, thus the fluid Cauchy-stress tensor is given by $\boldsymbol{\sigma}(\boldsymbol{u},p) \stackrel{\text{def}}{=} -p\boldsymbol{I}+2\mu\boldsymbol{\varepsilon}(\boldsymbol{u})$, with $\boldsymbol{\varepsilon}(\boldsymbol{u}) \stackrel{\text{def}}{=} \frac{1}{2}\left(\boldsymbol{\nabla u}+\boldsymbol{\nabla u}^{\mathrm{T}}\right)$ and where μ stands for the fluid dynamic viscosity. A given pressure data p_Γ is prescribed on Γ. At last, the surface differential operators $\left(\boldsymbol{L}^{\mathrm{e}}_{\boldsymbol{d}},\boldsymbol{L}^{\mathrm{e}}_{\boldsymbol{\theta}}\right)$ and $\left(\boldsymbol{L}^{\mathrm{v}}_{\boldsymbol{d}},\boldsymbol{L}^{\mathrm{v}}_{\boldsymbol{\theta}}\right)$ describe the shell elastic and viscous contributions, respectively.

Remark 1 *A commonly used expression for the viscous operator $\left(\boldsymbol{L}^{\mathrm{v}}_{\boldsymbol{d}},\boldsymbol{L}^{\mathrm{v}}_{\boldsymbol{\theta}}\right)$ is given by the so-called Rayleigh damping: $\boldsymbol{L}^{\mathrm{v}}_{\boldsymbol{d}}(\dot{\boldsymbol{d}},\dot{\boldsymbol{\theta}}) = \alpha\rho^{\mathrm{s}}\epsilon\dot{\boldsymbol{d}} + \beta D\boldsymbol{L}^{\mathrm{e}}_{\boldsymbol{d}}(\boldsymbol{d},\boldsymbol{\theta})(\dot{\boldsymbol{d}},\dot{\boldsymbol{\theta}})$, $\boldsymbol{L}^{\mathrm{v}}_{\boldsymbol{\theta}}(\dot{\boldsymbol{d}},\dot{\boldsymbol{\theta}}) = \beta D\boldsymbol{L}^{\mathrm{e}}_{\boldsymbol{\theta}}(\boldsymbol{d},\boldsymbol{\theta})(\dot{\boldsymbol{d}},\dot{\boldsymbol{\theta}})$, where $\alpha,\beta>0$ are given parameters and $D\boldsymbol{L}^{\mathrm{e}}_{\boldsymbol{d}}(\boldsymbol{d},\boldsymbol{\theta})$, $D\boldsymbol{L}^{\mathrm{e}}_{\boldsymbol{\theta}}(\boldsymbol{d},\boldsymbol{\theta})$ denote the Fréchet derivatives of $\boldsymbol{L}^{\mathrm{e}}_{\boldsymbol{d}},\boldsymbol{L}^{\mathrm{e}}_{\boldsymbol{\theta}}$ at $(\boldsymbol{d},\boldsymbol{\theta})$. For instance, in artery wall modeling, the zeroth-order term takes into account the dissipative effects of external tissue on blood vessels (see [31]), while the differential term can be viewed as a generalization of the Kelvin-Voigt model (see, e.g., [27, 6, 38])*

3 A class of fully decoupled schemes

In this section, we introduce time semi-discrete approximations of (1)-(2) which enable a fully decoupled time-marching of $(\boldsymbol{d}^{\mathrm{f}},\boldsymbol{u},p,\boldsymbol{d})$. Basically, the idea consists in combining the thin-walled nature of the structure with a velocity/pressure splitting of the fluid problem based on the Chorin-Temam projection scheme. In what follows, $\tau>0$ denotes the time-step size, $t_n \stackrel{\text{def}}{=} n\tau$, for $n\in\mathbb{N}$, and $\partial_\tau x^n \stackrel{\text{def}}{=} \left(x^n-x^{n-1}\right)/\tau$ the first order backward difference in time. We will make use of the superscript * to indicate zeroth- (i.e., without), first-order or second-order extrapolation from the previous time-steps, namely, $x^\star=0$ if $r=0$, $x^\star=x^{n-1}$ if $r=1$ and $x^\star=2x^{n-1}-x^{n-2}$ if $r=2$, where r denotes the extrapolation order. Using this notation, the proposed time semi-discrete approximations of (1)-(2) are reported in Algorithm 1. For the detailed derivation of the schemes the reader is referred to Section 4.

A salient feature of Algorithm 1 is its eminently explicit nature. The fluid domain geometry update is treated explicitly in the first step while, the three subsequent steps perform a fully decoupled sequential computation of $\boldsymbol{u}^n$, p^n and $\boldsymbol{d}^n$. We will see in Section 4.2 below that, for a representative linear setting, all this level of explicitness does not compromise energy stability. In fact, the key ingredient for stability is the underlying implicit fluid-pressure/solid-inertia coupling involved in the projection sub-step (5).

Another important aspect of the scheme is its intrinsic partitioned (or modular) character, in the sense that the overall fluid problem (3)-(5) does not depend on the specific structure of the solid model, and viceversa. In particular, the solid sub-step (6) is simply an implicit first-order time-discretization of the shell equations $(2)_{2-5}$ with a known forcing term. Note also that the interface Robin conditions $(4)_3$ and $(5)_3$ are nothing but that consistent relaxations of the kinematic compatibility $(2)_1$. In this sense, it is worth recalling that for pressure-correction Chorin-Temam fractional-step methods, Dirichlet conditions on the velocity yield the homogeneous Neumann conditions for the pressure (see, e.g., [22, 23]).

4 Derivation and analysis in the linear case

We consider a low Reynolds regime and assume that the structure undergoes infinitesimal displacements. The fluid can thus be described by the Stokes equations, in a fixed domain, and the structure by a linear visco-elastic Reissner-Mindlin shell model. In this framework, the coupled problem (1)-(2) reduces to: find the fluid velocity $\boldsymbol{u}:\Omega\times\mathbb{R}^+\to\mathbb{R}^3$, the fluid pressure $p:\Omega\times\mathbb{R}^+\to\mathbb{R}$, the solid displacement $\boldsymbol{d}:\Sigma\times\mathbb{R}^+\to\mathbb{R}^3$ and the rotation vector $\boldsymbol{\theta}:\Sigma\times\mathbb{R}^+\to\mathbb{R}^3$,

Algorithm 1 Fully decoupled schemes for (1)-(2)

For $n \geq r+1$:

1. Fluid domain update:

$$\boldsymbol{d}^{\mathrm{f},n} = \mathrm{Ext}(\boldsymbol{d}^{n-1}|_{\Sigma}), \quad \boldsymbol{w}^n = \partial_\tau \boldsymbol{d}^{\mathrm{f},n}, \quad \boldsymbol{\mathcal{A}}^n = \boldsymbol{I}_\Omega + \boldsymbol{d}^{\mathrm{f},n}, \quad \Omega^n = \boldsymbol{\mathcal{A}}^n\big(\Omega\big) \tag{3}$$

and then set $\boldsymbol{F}^n = \boldsymbol{\nabla}\boldsymbol{\mathcal{A}}^n, \quad J^n = \det \boldsymbol{F}^n$.

2. Fluid viscous sub-step: find $\boldsymbol{u}^n : \Omega^n \to \mathbb{R}^3$ such that

$$\begin{cases} \rho^{\mathrm{f}} \dfrac{\boldsymbol{u}^n - \boldsymbol{u}^{n-1}}{\tau}\Big|_{\boldsymbol{\mathcal{A}}} + \rho^{\mathrm{f}}\big(\boldsymbol{u}^{n-1} - \boldsymbol{w}^n\big)\cdot\boldsymbol{\nabla}\boldsymbol{u}^n - 2\mu\mathbf{div}\boldsymbol{\varepsilon}(\boldsymbol{u}^n) \\ \qquad\qquad +\boldsymbol{\nabla}p^{n-1} = \boldsymbol{0} \quad \text{in} \quad \Omega^n, \\ 2\mu\boldsymbol{\varepsilon}(\boldsymbol{u}^n)\boldsymbol{n} = \boldsymbol{0} \quad \text{on} \quad \Gamma, \\ 2\mu J^n\boldsymbol{\varepsilon}(\boldsymbol{u}^n)(\boldsymbol{F}^n)^{-\mathrm{T}}\boldsymbol{n} + \dfrac{\rho^{\mathrm{s}}\epsilon}{\tau}\boldsymbol{u}^n = \dfrac{\rho^{\mathrm{s}}\epsilon}{\tau}\big(\dot{\boldsymbol{d}}^{n-1} + \tau\partial_\tau\dot{\boldsymbol{d}}^\star_{\|}\big) \\ \qquad\qquad +(2\mu J\boldsymbol{\varepsilon}(\boldsymbol{u})(\boldsymbol{F})^{-\mathrm{T}}\boldsymbol{n})^\star_{\|} \quad \text{on} \quad \Sigma. \end{cases} \tag{4}$$

3. Fluid projection sub-step: find $p^n : \Omega^n \to \mathbb{R}$ such that

$$\begin{cases} -\dfrac{\tau}{\rho^{\mathrm{f}}}\Delta p^n = -\,\mathrm{div}\boldsymbol{u}^n & \text{in} \quad \Omega^n, \\ p^n = p_\Gamma & \text{on} \quad \Gamma, \\ \dfrac{\tau}{\rho^{\mathrm{f}}}\dfrac{\partial p^n}{\partial \boldsymbol{n}} + \dfrac{\tau}{\rho^{\mathrm{s}}\epsilon}p^n = \dfrac{\tau}{\rho^{\mathrm{s}}\epsilon}p^\star + \big(\boldsymbol{u}^\star - \dot{\boldsymbol{d}}^\star\big)\cdot\boldsymbol{n} & \text{on} \quad \Sigma. \end{cases} \tag{5}$$

4. Solid sub-step: find $\boldsymbol{d}^n : \Sigma \to \mathbb{R}^3$ and $\boldsymbol{\theta}^n : \Sigma \to \mathbb{R}^3$ with $\boldsymbol{\theta}^n_\perp = \boldsymbol{0}$ and such that

$$\begin{cases} \rho^{\mathrm{s}}\epsilon\partial_\tau\dot{\boldsymbol{d}}^n + \boldsymbol{L}^{\mathrm{e}}_{\boldsymbol{d}}(\boldsymbol{d}^n,\boldsymbol{\theta}^n) + \boldsymbol{L}^{\mathrm{v}}_{\boldsymbol{d}}(\dot{\boldsymbol{d}}^n,\dot{\boldsymbol{\theta}}^n) = -\,J^n\boldsymbol{\sigma}(\boldsymbol{u}^n,p^n)(\boldsymbol{F}^n)^{-\mathrm{T}}\boldsymbol{n} & \text{on} \quad \Sigma, \\ \boldsymbol{L}^{\mathrm{e}}_{\boldsymbol{\theta}}(\boldsymbol{d}^n,\boldsymbol{\theta}^n) + \boldsymbol{L}^{\mathrm{v}}_{\boldsymbol{\theta}}(\dot{\boldsymbol{d}}^n,\dot{\boldsymbol{\theta}}^n) = \boldsymbol{0} & \text{on} \quad \Sigma, \\ \dot{\boldsymbol{d}}^n = \partial_\tau\boldsymbol{d}^n, \quad \dot{\boldsymbol{\theta}}^n = \partial_\tau\boldsymbol{\theta}^n & \text{on} \quad \Sigma, \\ \boldsymbol{d}^n = \boldsymbol{\theta}^n = \boldsymbol{0} & \text{on} \quad \partial\Sigma. \end{cases} \tag{6}$$

---

with $\boldsymbol{\theta}_\perp = \boldsymbol{0}$, and such that

$$\begin{cases} \rho^{\mathrm{f}}\partial_t\boldsymbol{u} - \mathbf{div}\boldsymbol{\sigma}(\boldsymbol{u},p) = \boldsymbol{0} & \text{in} \quad \Omega, \\ \mathrm{div}\boldsymbol{u} = 0 & \text{in} \quad \Omega, \\ \boldsymbol{\sigma}(\boldsymbol{u},p)\boldsymbol{n} = -\,p_\Gamma\boldsymbol{n} & \text{on} \quad \Gamma, \end{cases} \tag{7}$$

$$\begin{cases} \boldsymbol{u} = \dot{\boldsymbol{d}} & \text{on} \quad \Sigma, \\ \rho^{\mathrm{s}}\epsilon\partial_t\dot{\boldsymbol{d}} + \boldsymbol{L}^{\mathrm{e}}_{\boldsymbol{d}}(\boldsymbol{d},\boldsymbol{\theta}) + \boldsymbol{L}^{\mathrm{v}}_{\boldsymbol{d}}(\dot{\boldsymbol{d}},\dot{\boldsymbol{\theta}}) = -\,\boldsymbol{\sigma}(\boldsymbol{u},p)\boldsymbol{n} & \text{on} \quad \Sigma, \\ \boldsymbol{L}^{\mathrm{e}}_{\boldsymbol{\theta}}(\boldsymbol{d},\boldsymbol{\theta}) + \boldsymbol{L}^{\mathrm{v}}_{\boldsymbol{\theta}}(\dot{\boldsymbol{d}},\dot{\boldsymbol{\theta}}) = \boldsymbol{0} & \text{on} \quad \Sigma, \\ \dot{\boldsymbol{d}} = \partial_t\boldsymbol{d}, \quad \dot{\boldsymbol{\theta}} = \partial_t\boldsymbol{\theta} & \text{on} \quad \Sigma, \\ \boldsymbol{d} = \boldsymbol{\theta} = \boldsymbol{0} & \text{on} \quad \partial\Sigma. \end{cases} \tag{8}$$

Here, the elastic and viscous solid operators, $\left(\boldsymbol{L}^{\mathrm{e}}_{\boldsymbol{d}}, \boldsymbol{L}^{\mathrm{e}}_{\boldsymbol{\theta}}\right)$ and $\left(\boldsymbol{L}^{\mathrm{v}}_{\boldsymbol{d}}, \boldsymbol{L}^{\mathrm{v}}_{\boldsymbol{\theta}}\right)$, are supposed to be linear.

Remark 2 *Though simplified, problem* (7)-(8) *retain some of the main numerical issues that appear in complex non-linear incompressible fluid-structure interaction problems.*

4.1 Time semi-discretization

This section is devoted to the time discretization of the coupled problem (7)-(8). The same considerations apply to the general non-linear problem (1)-(2). A fundamental feature of the coupled system (7)-(8) is its underlying Robin consistency on the interface, intimately related to thin-walled nature of the structure. More specifically, by inserting the kinematic coupling condition $(8)_1$ into the structure momentum equation $(8)_2$ we get the following expression

$$\boldsymbol{\sigma}(\boldsymbol{u}, p)\boldsymbol{n} + \rho^{\mathrm{s}}\epsilon\partial_t\boldsymbol{u} = -\boldsymbol{L}^{\mathrm{e}}_{\boldsymbol{d}}(\boldsymbol{d}, \boldsymbol{\theta}) - \boldsymbol{L}^{\mathrm{v}}_{\boldsymbol{d}}(\dot{\boldsymbol{d}}, \dot{\boldsymbol{\theta}}) \quad \text{on} \quad \Sigma, \tag{9}$$

which can be regarded as Robin-like boundary condition for the fluid (see, e.g., [32, 24, 14, 19]). This interface Robin consistency, has recently been used in the literature to avoid, without compromising optimal accuracy, the infamous unconditional instability issues of standard loosely coupled schemes (see [14, 19]). Basically, these methods split the time-marching of $(\boldsymbol{u}, p)$ and $\boldsymbol{d}$. The schemes proposed in this work enable the fully decoupled sequential computation of the whole fluid-solid state.

The solution procedures proposed in this paper rely on the following three ingredients:

1. Fractional-step time-marching of the fluid via the standard Chorin-Temam projection scheme (see, e.g, [23, 9, 37]):

   (a) Viscous-step:
   $$\begin{cases} \rho^{\mathrm{f}}\,\dfrac{\tilde{\boldsymbol{u}}^n - \boldsymbol{u}^{n-1}}{\tau} - 2\mu\mathbf{div}\boldsymbol{\varepsilon}(\tilde{\boldsymbol{u}}^n) = \boldsymbol{0} & \text{in} \quad \Omega, \\ 2\mu\boldsymbol{\varepsilon}(\tilde{\boldsymbol{u}}^n)\boldsymbol{n} = \boldsymbol{0} & \text{on} \quad \Gamma. \end{cases} \tag{10}$$

   (b) Projection-step:
   $$\begin{cases} \rho^{\mathrm{f}}\,\dfrac{\boldsymbol{u}^n - \tilde{\boldsymbol{u}}^n}{\tau} + \boldsymbol{\nabla}p^n = \boldsymbol{0} & \text{in} \quad \Omega, \\ \mathrm{div}\boldsymbol{u}^n = 0 & \text{in} \quad \Omega, \\ p^n = p_\Gamma & \text{on} \quad \Gamma. \end{cases} \tag{11}$$

2. Explicit interface conditions for (10) and (11), based on a specific fractional-step time-marching of (9), which preserve the velocity/pressure splitting and treat implicitly the solid-inertia contributions.

3. Fluid stresses are transmitted to the solid by solving the standard problem:
   $$\begin{cases} \rho^{\mathrm{s}}\epsilon\partial_\tau\dot{\boldsymbol{d}}^n + \boldsymbol{L}^{\mathrm{e}}_{\boldsymbol{d}}(\boldsymbol{d}^n, \boldsymbol{\theta}^n) + \boldsymbol{L}^{\mathrm{v}}_{\boldsymbol{d}}(\dot{\boldsymbol{d}}^n, \dot{\boldsymbol{\theta}}^n) = -\boldsymbol{\sigma}(\tilde{\boldsymbol{u}}^n, p^n)\boldsymbol{n} & \text{on} \quad \Sigma, \\ \boldsymbol{L}^{\mathrm{e}}_{\boldsymbol{\theta}}(\boldsymbol{d}^n, \boldsymbol{\theta}^n) + \boldsymbol{L}^{\mathrm{v}}_{\boldsymbol{\theta}}(\dot{\boldsymbol{d}}^n, \dot{\boldsymbol{\theta}}^n) = \boldsymbol{0} & \text{on} \quad \Sigma, \\ \dot{\boldsymbol{d}} = \partial_\tau\boldsymbol{d}^n, \quad \dot{\boldsymbol{\theta}}^n = \partial_\tau\boldsymbol{\theta}^n & \text{on} \quad \Sigma, \\ \boldsymbol{d}^n = \boldsymbol{\theta}^n = \boldsymbol{0} & \text{on} \quad \partial\Sigma. \end{cases} \tag{12}$$

We now further elaborate on the second point. We first note that the projection-step (11) only contributes to the normal component of the fluid-stress, that is, $-p = \boldsymbol{\sigma}(\boldsymbol{u}, p)\boldsymbol{n} \cdot \boldsymbol{n}$. This

is consistent with the fact that, in (11), only the normal component of the velocity has a well-defined trace on Σ. In terms of interface coupling, this indicates that the projection-step only contributes to the normal component of (9). Therefore, its tangential component has to be taken into account in the viscous-step (10). We therefore propose the following two-stage time discretization of (9):

$$\begin{cases} 2\mu\boldsymbol{\varepsilon}(\tilde{\boldsymbol{u}}^n)\boldsymbol{n} + \dfrac{\rho^{\mathrm{s}}\epsilon}{\tau}\tilde{\boldsymbol{u}}^n = \dfrac{\rho^{\mathrm{s}}\epsilon}{\tau}\dot{\boldsymbol{d}}^{n-1} - \boldsymbol{L}^{\mathrm{e}}_{\boldsymbol{d}}(\boldsymbol{d}^\star,\boldsymbol{\theta}^\star)_{\|} - \boldsymbol{L}^{\mathrm{v}}_{\boldsymbol{d}}(\dot{\boldsymbol{d}}^\star,\dot{\boldsymbol{\theta}}^\star)_{\|} & \text{on} \quad \Sigma, \\ -p^n + \dfrac{\rho^{\mathrm{s}}\epsilon}{\tau}\boldsymbol{u}^n\cdot\boldsymbol{n} = \dfrac{\rho^{\mathrm{s}}\epsilon}{\tau}\tilde{\boldsymbol{u}}^n\cdot\boldsymbol{n} - \boldsymbol{L}^{\mathrm{e}}_{\boldsymbol{d}}(\boldsymbol{d}^\star,\boldsymbol{\theta}^\star)\cdot\boldsymbol{n} - \boldsymbol{L}^{\mathrm{v}}_{\boldsymbol{d}}(\dot{\boldsymbol{d}}^\star,\dot{\boldsymbol{\theta}}^\star)\cdot\boldsymbol{n} & \text{on} \quad \Sigma. \end{cases} \tag{13}$$

These interface relations preserve the original splitting of (10) and (11) and enable the interface fluid-solid splitting through the explicit treatment of the solid viscoelastic terms in (13). Besides, these extrapolations are performed to control the perturbation of the kinematic coupling, which dramatically affects accuracy in practice (see Section 5 and [14, 19]).

In summary, a three-stage splitting of the coupled problem (7)-(8) can be performed by solving (10) with $(13)_1$, then (11) with $(13)_2$ and finally (12). The fully decoupled schemes proposed in this paper combine this approach with two additional refinements. First, in order to avoid the annoying extrapolations of the solid viscoelastic terms in (13), we instead consider the following equivalent interface relations

$$\begin{cases} 2\mu\boldsymbol{\varepsilon}(\boldsymbol{u}^n)\boldsymbol{n} + \dfrac{\rho^{\mathrm{s}}\epsilon}{\tau}\boldsymbol{u}^n = \dfrac{\rho^{\mathrm{s}}\epsilon}{\tau}\big(\dot{\boldsymbol{d}}^{n-1} + \tau\partial_\tau\dot{\boldsymbol{d}}^\star_{\|}\big) + (2\mu\boldsymbol{\varepsilon}(\tilde{\boldsymbol{u}}^\star)\boldsymbol{n})_{\|} & \text{on} \quad \Sigma, \\ -p^n + \dfrac{\rho^{\mathrm{s}}\epsilon}{\tau}\boldsymbol{u}^n\cdot\boldsymbol{n} = \dfrac{\rho^{\mathrm{s}}\epsilon}{\tau}\tilde{\boldsymbol{u}}^n\cdot\boldsymbol{n} - p^\star + \dfrac{\rho^{\mathrm{s}}\epsilon}{\tau}\Big(\dot{\boldsymbol{d}}^\star - \tilde{\boldsymbol{u}}^\star\Big)\cdot\boldsymbol{n} & \text{on} \quad \Sigma \end{cases} \tag{14}$$

for $n \geq r+1$. To this purpose, we first note that from $(12)_1$ it follows that

$$-\boldsymbol{L}^{\mathrm{e}}_{\boldsymbol{d}}(\boldsymbol{d}^\star,\boldsymbol{\theta}^\star) - \boldsymbol{L}^{\mathrm{v}}_{\boldsymbol{d}}(\dot{\boldsymbol{d}}^\star,\dot{\boldsymbol{\theta}}^\star) = \rho^{\mathrm{s}}\epsilon\partial_\tau\dot{\boldsymbol{d}}^\star + \boldsymbol{\sigma}(\tilde{\boldsymbol{u}}^\star,p^\star)\boldsymbol{n} \tag{15}$$

for $n \geq r+1$. The relation $(14)_1$ simply follows by inserting the tangential component of (15) into $(13)_1$. Similarly, by combining (15) with $(14)_1$ we infer that

$$\begin{aligned} -\boldsymbol{L}^{\mathrm{e}}_{\boldsymbol{d}}(\boldsymbol{d}^\star,\boldsymbol{\theta}^\star)\cdot\boldsymbol{n} - \boldsymbol{L}^{\mathrm{v}}_{\boldsymbol{d}}(\dot{\boldsymbol{d}}^\star,\dot{\boldsymbol{\theta}}^\star)\cdot\boldsymbol{n} &= -p^\star + \rho^{\mathrm{s}}\epsilon\partial_\tau\dot{\boldsymbol{d}}^\star\cdot\boldsymbol{n} - \frac{\rho^{\mathrm{s}}\epsilon}{\tau}\Big(\tilde{\boldsymbol{u}}^\star - \dot{\boldsymbol{d}}^{\star-1}\Big)\cdot\boldsymbol{n} \\ &= -p^\star + \frac{\rho^{\mathrm{s}}\epsilon}{\tau}\Big(\dot{\boldsymbol{d}}^\star - \tilde{\boldsymbol{u}}^\star\Big)\cdot\boldsymbol{n}. \end{aligned}$$

By inserting this expression into $(13)_2$ we get $(14)_2$. At last, instead of the Darcy-step (11), we consider the equivalent pressure-Poisson formulation complemented with the following interface Robin condition, derived from $(14)_2$:

$$\frac{\tau}{\rho^{\mathrm{f}}}\frac{\partial p^n}{\partial\boldsymbol{n}} = -(\boldsymbol{u}^n - \tilde{\boldsymbol{u}}^n)\cdot\boldsymbol{n} = \frac{\tau}{\rho^{\mathrm{s}}\epsilon}(p^\star - p^n) + \big(\tilde{\boldsymbol{u}}^\star - \dot{\boldsymbol{d}}^\star\big)\cdot\boldsymbol{n} \quad \text{on} \quad \Sigma.$$

The proposed fully decoupled schemes for problem (7)-(8) are detailed in Algorithm 2. Note that, for $r = 1$ and 2, the schemes are multi-steps methods ($n \geq r+1$). The additional data needed to start the time-marching can be generated, for instance, by performing one step of the scheme with $r = 0$, which yields , $\dot{\boldsymbol{d}}^1$, and then one step of the scheme with $r = 1$, which gives $\dot{\boldsymbol{d}}^2$.

4.2 Stability analysis

In this section, we provide an energy based estimate for Algorithm 2 with $r = 0$ and $r = 1$.

Algorithm 2 Fully decoupled schemes for (7)-(8)

For $n \geq r+1$:

1. Fluid viscous sub-step: find $\tilde{\boldsymbol{u}}^n : \Omega \to \mathbb{R}^d$ such that

$$\begin{cases} \rho^{\mathrm{f}} \dfrac{\tilde{\boldsymbol{u}}^n - \boldsymbol{u}^{n-1}}{\tau} - 2\mu \mathbf{div}\boldsymbol{\varepsilon}(\tilde{\boldsymbol{u}}^n) = \boldsymbol{0} & \text{in} \quad \Omega, \\ 2\mu\boldsymbol{\varepsilon}(\boldsymbol{u}^n)\boldsymbol{n} = \boldsymbol{0} & \text{on} \quad \Gamma, \\ 2\mu\boldsymbol{\varepsilon}(\boldsymbol{u}^n)\boldsymbol{n} + \dfrac{\rho^{\mathrm{s}}\epsilon}{\tau}\boldsymbol{u}^n = \dfrac{\rho^{\mathrm{s}}\epsilon}{\tau}\big(\dot{\boldsymbol{d}}^{n-1} + \tau\partial_\tau \dot{\boldsymbol{d}}^\star_{\|}\big) + (2\mu\boldsymbol{\varepsilon}(\tilde{\boldsymbol{u}}^\star)\boldsymbol{n})_{\|} & \text{on} \quad \Sigma. \end{cases} \tag{16}$$

2. Fluid projection sub-step: find $p^n : \Omega \to \mathbb{R}$ such that

$$\begin{cases} -\dfrac{\tau}{\rho^{\mathrm{f}}}\Delta p^n = -\operatorname{div}\tilde{\boldsymbol{u}}^n & \text{in} \quad \Omega, \\ p^n = p_\Gamma & \text{on} \quad \Gamma, \\ \dfrac{\tau}{\rho^{\mathrm{f}}}\dfrac{\partial p^n}{\partial \boldsymbol{n}} + \dfrac{\tau}{\rho^{\mathrm{s}}\epsilon}p^n = \dfrac{\tau}{\rho^{\mathrm{s}}\epsilon}p^\star + \big(\tilde{\boldsymbol{u}}^\star - \dot{\boldsymbol{d}}^\star\big)\cdot\boldsymbol{n} & \text{on} \quad \Sigma. \end{cases} \tag{17}$$

   Thereafter set $\boldsymbol{u}^n = \tilde{\boldsymbol{u}}^n - \frac{\tau}{\rho^{\mathrm{f}}}\boldsymbol{\nabla} p^n$.

3. Solid sub-step: find $\boldsymbol{d}^n : \Sigma \to \mathbb{R}^3$ and $\boldsymbol{\theta}^n : \Sigma \to \mathbb{R}^3$ with $\boldsymbol{\theta}^n_\perp = \boldsymbol{0}$ and such that

$$\begin{cases} \rho^{\mathrm{s}}\epsilon\partial_\tau \dot{\boldsymbol{d}}^n + \boldsymbol{L}^{\mathrm{e}}_{\boldsymbol{d}}(\boldsymbol{d}^n, \boldsymbol{\theta}^n) + \boldsymbol{L}^{\mathrm{v}}_{\boldsymbol{d}}(\dot{\boldsymbol{d}}^n, \dot{\boldsymbol{\theta}}^n) = -\boldsymbol{\sigma}(\tilde{\boldsymbol{u}}^n, p^n)\boldsymbol{n} & \text{in} \quad \Sigma, \\ \boldsymbol{L}^{\mathrm{e}}_{\boldsymbol{\theta}}(\boldsymbol{d}^n, \boldsymbol{\theta}^n) + \boldsymbol{L}^{\mathrm{v}}_{\boldsymbol{\theta}}(\dot{\boldsymbol{d}}^n, \dot{\boldsymbol{\theta}}^n) = \boldsymbol{0} & \text{on} \quad \Sigma, \\ \dot{\boldsymbol{d}}^n = \partial_\tau \boldsymbol{d}^n, \quad \dot{\boldsymbol{\theta}}^n = \partial_\tau \boldsymbol{\theta}^n & \text{on} \quad \Sigma, \\ \boldsymbol{d}^n = \boldsymbol{\theta}^n = \boldsymbol{0} & \text{on} \quad \partial\Sigma. \end{cases} \tag{18}$$

4.2.1 Preliminaries

Let ω be a given domain or surface in $\mathbb{R}^3$. In the succeeding text, the scalar product in $L^2(\omega)$ is denoted by $(\cdot,\cdot)_\omega$ and its norm by $\|\cdot\|_\omega$. Since the elastic and viscous solid surface operators, $\big(\boldsymbol{L}^{\mathrm{e}}_{\boldsymbol{d}}, \boldsymbol{L}^{\mathrm{e}}_{\boldsymbol{\theta}}\big)$ and $\big(\boldsymbol{L}^{\mathrm{v}}_{\boldsymbol{d}}, \boldsymbol{L}^{\mathrm{v}}_{\boldsymbol{\theta}}\big)$, are supposed to be linear, they admit the following decomposition:

$$\begin{aligned} \boldsymbol{L}^{\mathrm{e}}_{\boldsymbol{d}}(\boldsymbol{d},\boldsymbol{\theta}) &\stackrel{\text{def}}{=} \boldsymbol{A}^{\mathrm{e}}_{\boldsymbol{d}}\boldsymbol{d} + \boldsymbol{B}^{\mathrm{e}}_{\boldsymbol{d}}\boldsymbol{\theta}, \quad \boldsymbol{L}^{\mathrm{v}}_{\boldsymbol{d}}(\boldsymbol{d},\boldsymbol{\theta}) \stackrel{\text{def}}{=} \boldsymbol{A}^{\mathrm{v}}_{\boldsymbol{d}}\boldsymbol{d} + \boldsymbol{B}^{\mathrm{v}}_{\boldsymbol{d}}\boldsymbol{\theta}, \\ \boldsymbol{L}^{\mathrm{e}}_{\boldsymbol{\theta}}(\boldsymbol{d},\boldsymbol{\theta}) &\stackrel{\text{def}}{=} \boldsymbol{B}^{\mathrm{e}}_{\boldsymbol{\theta}}\boldsymbol{d} + \boldsymbol{C}^{\mathrm{e}}_{\boldsymbol{\theta}}\boldsymbol{\theta}, \quad \boldsymbol{L}^{\mathrm{v}}_{\boldsymbol{\theta}}(\boldsymbol{d},\boldsymbol{\theta}) \stackrel{\text{def}}{=} \boldsymbol{B}^{\mathrm{v}}_{\boldsymbol{\theta}}\boldsymbol{d} + \boldsymbol{C}^{\mathrm{v}}_{\boldsymbol{\theta}}\boldsymbol{\theta}. \end{aligned}$$

We assume that the corresponding matrix operators

$$\boldsymbol{Q}^{\mathrm{e}} \stackrel{\text{def}}{=} \begin{bmatrix} \boldsymbol{A}^{\mathrm{e}}_{\boldsymbol{d}} & \boldsymbol{B}^{\mathrm{e}}_{\boldsymbol{d}} \\ \boldsymbol{B}^{\mathrm{e}}_{\boldsymbol{\theta}} & \boldsymbol{C}^{\mathrm{e}}_{\boldsymbol{\theta}} \end{bmatrix}, \quad \boldsymbol{Q}^{\mathrm{v}} \stackrel{\text{def}}{=} \begin{bmatrix} \boldsymbol{A}^{\mathrm{v}}_{\boldsymbol{d}} & \boldsymbol{B}^{\mathrm{v}}_{\boldsymbol{d}} \\ \boldsymbol{B}^{\mathrm{v}}_{\boldsymbol{\theta}} & \boldsymbol{C}^{\mathrm{v}}_{\boldsymbol{\theta}} \end{bmatrix},$$

are self-adjoint positive definite operators in $[L^2(\Sigma)]^3 \times [L^2(\Sigma)]^3$. The following notation will be used

$$\boldsymbol{y} \stackrel{\text{def}}{=} \begin{bmatrix} \boldsymbol{d} \\ \boldsymbol{\theta} \end{bmatrix}, \quad \dot{\boldsymbol{y}} \stackrel{\text{def}}{=} \begin{bmatrix} \dot{\boldsymbol{d}} \\ \dot{\boldsymbol{\theta}} \end{bmatrix}$$

and their corresponding elastic-energy and viscous-dissipation norms

$$\|\boldsymbol{y}\|_{\mathrm{e}} \stackrel{\mathrm{def}}{=} \left(\boldsymbol{Q}^{\mathrm{e}}\boldsymbol{y},\boldsymbol{y}\right)_{\Sigma}^{\frac{1}{2}}, \quad \|\dot{\boldsymbol{y}}\|_{\mathrm{v}} \stackrel{\mathrm{def}}{=} \left(\boldsymbol{Q}^{\mathrm{v}}\dot{\boldsymbol{y}},\dot{\boldsymbol{y}}\right)_{\Sigma}^{\frac{1}{2}}.$$

In order to ease the presentation, we will commit a slight abuse of notation by settting $\boldsymbol{L}^{\mathrm{e}}_{\boldsymbol{d}}\boldsymbol{y} \stackrel{\mathrm{def}}{=} \boldsymbol{L}^{\mathrm{e}}_{\boldsymbol{d}}(\boldsymbol{d},\boldsymbol{\theta})$ and $\boldsymbol{L}^{\mathrm{v}}_{\boldsymbol{d}}\dot{\boldsymbol{y}} \stackrel{\mathrm{def}}{=} \boldsymbol{L}^{\mathrm{v}}_{\boldsymbol{d}}(\dot{\boldsymbol{d}},\dot{\boldsymbol{\theta}})$. The same applies to the operators $\boldsymbol{L}^{\mathrm{e}}_{\boldsymbol{\theta}}$ and $\boldsymbol{L}^{\mathrm{v}}_{\boldsymbol{\theta}}$. Finally, we define the time semi-discrete energy E^n and dissipation D^n, at time-step t_n, by

$$E^n \stackrel{\mathrm{def}}{=} \frac{\rho^{\mathrm{f}}}{2}\|\boldsymbol{u}^n\|^2_{\Omega} + \frac{\rho^{\mathrm{s}}\epsilon}{2}\|\dot{\boldsymbol{d}}^n\|^2_{\Sigma} + \frac{1}{2}\|\boldsymbol{y}^n\|^2_{\mathrm{e}}, \quad D^n \stackrel{\mathrm{def}}{=} 2\mu\tau\|\boldsymbol{\varepsilon}(\tilde{\boldsymbol{u}}^n)\|^2_{\Omega} + \tau\|\dot{\boldsymbol{y}}^n\|^2_{\mathrm{v}}.$$

4.2.2 A priori energy estimate

The following result states the unconditional stability of the fully decoupled time-marching schemes provided by Algorithm 2 with $r = 0$ or $r = 1$.

Theorem 1 *Assume that the system is isolated, i.e., $p_\Gamma = 0$ (free system) and let the sequence $\left\{(\tilde{\boldsymbol{u}}^n, \boldsymbol{u}^n, p^n, \boldsymbol{d}^n, \dot{\boldsymbol{d}}^n, \boldsymbol{\theta}^n, \dot{\boldsymbol{\theta}}^n)\right\}_{n\geq r+1}$ be given by Algorithm 2 with $r = 0$ or $r = 1$. The following a priori energy estimate holds for $n \geq r + 1$:*

$$E^n + \sum_{m=r+1}^{n} D^m \leq E^0. \tag{19}$$

Proof. We first reformulate the second step of Algorithm 2 as the following equivalent Darcy-problem:

$$\begin{cases} \rho^{\mathrm{f}}\,\dfrac{\boldsymbol{u}^n - \tilde{\boldsymbol{u}}^n}{\tau} + \boldsymbol{\nabla} p^n = \boldsymbol{0} \quad \text{in} \quad \Omega, \\ \mathrm{div}\boldsymbol{u}^n = 0 \quad \text{in} \quad \Omega, \\ p^n = p_\Gamma \quad \text{on} \quad \Gamma, \\ p^n + \dfrac{\rho^{\mathrm{s}}\epsilon}{\tau}\boldsymbol{u}^n\cdot\boldsymbol{n} = \dfrac{\rho^{\mathrm{s}}\epsilon}{\tau}\tilde{\boldsymbol{u}}^n\cdot\boldsymbol{n} - p^\star + \dfrac{\rho^{\mathrm{s}}\epsilon}{\tau}\left(\dot{\boldsymbol{d}}^\star - \tilde{\boldsymbol{u}}^\star\right)\cdot\boldsymbol{n} \quad \text{on} \quad \Sigma. \end{cases} \tag{20}$$

Note that, from $(16)_3$, $(18)_1$ and $(20)_4$, it follows that (13) holds for $n \geq r + 1$. Thus, by adding $(13)_1$ to $(13)_2$ multiplied by $\boldsymbol{n}$, we get

$$\frac{\rho^{\mathrm{s}}\epsilon}{\tau}\left((\tilde{\boldsymbol{u}}^n_{\parallel} + \boldsymbol{u}^n_{\perp}) - \dot{\boldsymbol{d}}^{n-1}\right) + \boldsymbol{L}^{\mathrm{e}}_{\boldsymbol{d}}\boldsymbol{y}^\star + \boldsymbol{L}^{\mathrm{v}}_{\boldsymbol{d}}\dot{\boldsymbol{y}}^\star = -\boldsymbol{\sigma}(\tilde{\boldsymbol{u}}^n, p^n)\boldsymbol{n} \quad \text{on} \quad \Sigma,$$

which, after subtraction from $(18)_1$, yields the following displacement-velocity correction reformulation of the solid step:

$$\frac{\rho^{\mathrm{s}}\epsilon}{\tau}\left(\dot{\boldsymbol{d}}^n - \left(\tilde{\boldsymbol{u}}^n_{\parallel} + \boldsymbol{u}^n_{\perp}\right)\right) + \boldsymbol{L}^{\mathrm{e}}_{\boldsymbol{d}}(\boldsymbol{y}^n - \boldsymbol{y}^\star) + \boldsymbol{L}^{\mathrm{v}}_{\boldsymbol{d}}(\dot{\boldsymbol{y}}^n - \dot{\boldsymbol{y}}^\star) = \boldsymbol{0} \quad \text{on} \quad \Sigma \tag{21}$$

for $n \geq r + 1$.

As a result, from $(13)_2$ and (21), we obtain the following perturbed kinematic constraints on the interface Σ:

$$\begin{cases} \boldsymbol{u}^n\cdot\boldsymbol{n} = \tilde{\boldsymbol{u}}^n\cdot\boldsymbol{n} + \dfrac{\tau}{\rho^{\mathrm{s}}\epsilon}(p^n - \boldsymbol{L}^{\mathrm{e}}_{\boldsymbol{d}}\boldsymbol{y}^\star\cdot\boldsymbol{n} - \boldsymbol{L}^{\mathrm{v}}_{\boldsymbol{d}}\dot{\boldsymbol{y}}^\star\cdot\boldsymbol{n}), \\ \tilde{\boldsymbol{u}}^n = \dot{\boldsymbol{d}}^n + \dfrac{\tau}{\rho^{\mathrm{s}}\epsilon}\left(\boldsymbol{L}^{\mathrm{e}}_{\boldsymbol{d}}(\boldsymbol{y}^n - \boldsymbol{y}^\star) + \boldsymbol{L}^{\mathrm{v}}_{\boldsymbol{d}}(\dot{\boldsymbol{y}}^n - \dot{\boldsymbol{y}}^\star)\right) \\ \qquad - \dfrac{\tau}{\rho^{\mathrm{s}}\epsilon}\left(p^n\boldsymbol{n} - \left(\boldsymbol{L}^{\mathrm{e}}_{\boldsymbol{d}}\boldsymbol{y}^\star\right)_\perp - \left(\boldsymbol{L}^{\mathrm{v}}_{\boldsymbol{d}}\dot{\boldsymbol{y}}^\star\right)_\perp\right) \end{cases} \tag{22}$$

for $n \geq r+1$.

We now proceed by taking the scalar product of $(16)_1$ and $(20)_1$ with $\tilde{\boldsymbol{u}}^n$ and $\boldsymbol{u}^n$, respectively. Hence, after integration by parts over Ω and summation of the resulting expressions, this yields

$$\frac{\rho^{\mathrm{f}}}{2\tau}\left(\|\boldsymbol{u}^n\|_\Omega^2 - \|\boldsymbol{u}^{n-1}\|_\Omega^2\right) + 2\mu\|\boldsymbol{\varepsilon}(\tilde{\boldsymbol{u}}^n)\|_\Omega^2 - (2\mu\boldsymbol{\varepsilon}(\tilde{\boldsymbol{u}}^n)\boldsymbol{n}, \tilde{\boldsymbol{u}}^n)_\Sigma + (p^n, \boldsymbol{u}^n\cdot\boldsymbol{n})_\Sigma \leq 0.$$

By inserting $(22)_1$ into the last term, we have

$$\begin{aligned}\frac{\rho^{\mathrm{f}}}{2\tau}\left(\|\boldsymbol{u}^n\|_\Omega^2 - \|\boldsymbol{u}^{n-1}\|_\Omega^2\right) + 2\mu\|\boldsymbol{\varepsilon}(\tilde{\boldsymbol{u}}^n)\|_\Omega^2 - (\boldsymbol{\sigma}(\tilde{\boldsymbol{u}}^n, p^n)\boldsymbol{n}, \tilde{\boldsymbol{u}}^n)_\Sigma \\ + \frac{\tau}{\rho^{\mathrm{s}}\epsilon}\left(p^n\boldsymbol{n}, p^n\boldsymbol{n} - \left(\boldsymbol{L}_{\boldsymbol{d}}^{\mathrm{e}}\boldsymbol{y}^\star\right)_\perp - \left(\boldsymbol{L}_{\boldsymbol{d}}^{\mathrm{v}}\dot{\boldsymbol{y}}^\star\right)_\perp\right)_\Sigma \leq 0.\end{aligned} \tag{23}$$

On the other hand, owing to $(18)_1$ and $(22)_2$, we infer that

$$\begin{aligned}-(\boldsymbol{\sigma}(\tilde{\boldsymbol{u}}^n, p^n)\boldsymbol{n}, \tilde{\boldsymbol{u}}^n)_\Sigma &= \frac{\rho^{\mathrm{s}}\epsilon}{2\tau}\left(\|\dot{\boldsymbol{d}}^n\|_\Sigma^2 - \|\dot{\boldsymbol{d}}^{n-1}\|_\Sigma^2 + \|\dot{\boldsymbol{d}}^n - \dot{\boldsymbol{d}}^{n-1}\|_\Sigma^2\right) + \underbrace{\left(\boldsymbol{L}_{\boldsymbol{d}}^{\mathrm{e}}\boldsymbol{y}^n + \boldsymbol{L}_{\boldsymbol{d}}^{\mathrm{v}}\dot{\boldsymbol{y}}^n, \dot{\boldsymbol{d}}^n\right)_\Sigma}_{T_0} \\ &+ \underbrace{\frac{\tau}{2\rho^{\mathrm{s}}\epsilon}\left(\|\boldsymbol{L}_{\boldsymbol{d}}^{\mathrm{e}}\boldsymbol{y}^n + \boldsymbol{L}_{\boldsymbol{d}}^{\mathrm{v}}\dot{\boldsymbol{y}}^n\|_\Sigma^2 - \|\boldsymbol{L}_{\boldsymbol{d}}^{\mathrm{e}}\boldsymbol{y}^\star + \boldsymbol{L}_{\boldsymbol{d}}^{\mathrm{v}}\dot{\boldsymbol{y}}^\star\|_\Sigma^2 + \|\boldsymbol{L}_{\boldsymbol{d}}^{\mathrm{e}}(\boldsymbol{y}^n - \boldsymbol{y}^\star) + \boldsymbol{L}_{\boldsymbol{d}}^{\mathrm{v}}(\dot{\boldsymbol{y}}^n - \dot{\boldsymbol{y}}^\star)\|_\Sigma^2\right)}_{T_1} \\ &+ \underbrace{\left(\dot{\boldsymbol{d}}^n - \dot{\boldsymbol{d}}^{n-1}, \boldsymbol{L}_{\boldsymbol{d}}^{\mathrm{e}}(\boldsymbol{y}^n - \boldsymbol{y}^\star) + \boldsymbol{L}_{\boldsymbol{d}}^{\mathrm{v}}(\dot{\boldsymbol{y}}^n - \dot{\boldsymbol{y}}^\star)\right)_\Sigma}_{T_2} \underbrace{- \left(\dot{\boldsymbol{d}}^n - \dot{\boldsymbol{d}}^{n-1}, p^n\boldsymbol{n} - \left(\boldsymbol{L}_{\boldsymbol{d}}^{\mathrm{e}}\boldsymbol{y}^\star\right)_\perp - \left(\boldsymbol{L}_{\boldsymbol{d}}^{\mathrm{v}}\dot{\boldsymbol{y}}^\star\right)_\perp\right)_\Sigma}_{T_3} \\ &- \frac{\tau}{\rho^{\mathrm{s}}\epsilon}\left(\boldsymbol{L}_{\boldsymbol{d}}^{\mathrm{e}}\boldsymbol{y}^n + \boldsymbol{L}_{\boldsymbol{d}}^{\mathrm{v}}\dot{\boldsymbol{y}}^n, p^n\boldsymbol{n} - \left(\boldsymbol{L}_{\boldsymbol{d}}^{\mathrm{e}}\boldsymbol{y}^\star\right)_\perp - \left(\boldsymbol{L}_{\boldsymbol{d}}^{\mathrm{v}}\dot{\boldsymbol{y}}^\star\right)_\perp\right)_\Sigma.\end{aligned} \tag{24}$$

Note that, thanks to $(18)_2$, for the term T_0 we have

$$\begin{aligned}T_0 &= \left(\boldsymbol{L}_{\boldsymbol{d}}^{\mathrm{e}}\boldsymbol{y}^n + \boldsymbol{L}_{\boldsymbol{d}}^{\mathrm{v}}\dot{\boldsymbol{y}}^n, \dot{\boldsymbol{d}}^n\right)_\Sigma + \left(\boldsymbol{L}_{\boldsymbol{\theta}}^{\mathrm{e}}\boldsymbol{y}^n + \boldsymbol{L}_{\boldsymbol{\theta}}^{\mathrm{v}}\dot{\boldsymbol{y}}^n, \dot{\boldsymbol{\theta}}^n\right)_\Sigma \\ &= (\boldsymbol{Q}^{\mathrm{e}}\dot{\boldsymbol{y}}^n, \boldsymbol{y}^n)_\Sigma + (\boldsymbol{Q}^{\mathrm{v}}\dot{\boldsymbol{y}}^n, \dot{\boldsymbol{y}}^n)_\Sigma \\ &= \frac{1}{2\tau}\left(\|\boldsymbol{y}^n\|_{\mathrm{e}}^2 - \left\|\boldsymbol{y}^{n-1}\right\|_{\mathrm{e}}^2 + \left\|\boldsymbol{y}^n - \boldsymbol{y}^{n-1}\right\|_{\mathrm{e}}^2\right) + \|\dot{\boldsymbol{y}}^n\|_{\mathrm{v}}^2.\end{aligned} \tag{25}$$

Hence, by inserting (25) into (24) and the resulting expression into (23), we get the following energy inequality

$$\begin{aligned}\frac{\rho^{\mathrm{f}}}{2\tau}\left(\|\boldsymbol{u}^n\|_\Omega^2 - \|\boldsymbol{u}^{n-1}\|_\Omega^2\right) + 2\mu\|\boldsymbol{\varepsilon}(\tilde{\boldsymbol{u}}^n)\|_\Omega^2 + \frac{\rho^{\mathrm{s}}\epsilon}{2\tau}\left(\|\dot{\boldsymbol{d}}^n\|_\Sigma^2 - \|\dot{\boldsymbol{d}}^{n-1}\|_\Sigma^2 + \|\dot{\boldsymbol{d}}^n - \dot{\boldsymbol{d}}^{n-1}\|_\Sigma^2\right) \\ + \frac{1}{2\tau}\left(\|\boldsymbol{y}^n\|_{\mathrm{e}}^2 - \left\|\boldsymbol{y}^{n-1}\right\|_{\mathrm{e}}^2 + \left\|\boldsymbol{y}^n - \boldsymbol{y}^{n-1}\right\|_{\mathrm{e}}^2\right) + \|\dot{\boldsymbol{y}}^n\|_{\mathrm{v}}^2 + T_1 + T_2 + T_3 \\ + \underbrace{\frac{\tau}{\rho^{\mathrm{s}}\epsilon}\left(p^n\boldsymbol{n} - \boldsymbol{L}_{\boldsymbol{d}}^{\mathrm{e}}\boldsymbol{y}^n - \boldsymbol{L}_{\boldsymbol{d}}^{\mathrm{v}}\dot{\boldsymbol{y}}^n, p^n\boldsymbol{n} - \left(\boldsymbol{L}_{\boldsymbol{d}}^{\mathrm{e}}\boldsymbol{y}^\star\right)_\perp - \left(\boldsymbol{L}_{\boldsymbol{d}}^{\mathrm{v}}\dot{\boldsymbol{y}}^\star\right)_\perp\right)_\Sigma}_{T_4} \leq 0\end{aligned} \tag{26}$$

for $n \geq r+1$.

We proceed by treating each case of extrapolation, $r=0$ or $r=1$, serarately.

Case $r = 0$. We have

$$T_2 + T_3 \geq -\frac{\rho^{\mathrm{s}}\epsilon}{2\tau}\|\dot{\boldsymbol{d}}^n - \dot{\boldsymbol{d}}^{n-1}\|_\Sigma^2 - \frac{\tau}{2\rho^{\mathrm{s}}\epsilon}\|\boldsymbol{L}_{\boldsymbol{d}}^{\mathrm{e}}\boldsymbol{y}^n + \boldsymbol{L}_{\boldsymbol{d}}^{\mathrm{v}}\dot{\boldsymbol{y}}^n - p^n\boldsymbol{n}\|_\Sigma^2$$

and

$$T_1 + T_4 = \frac{\tau}{2\rho^{\mathrm{s}}\epsilon}\|p^n\|_\Sigma^2 + \frac{\tau}{2\rho^{\mathrm{s}}\epsilon}\|\boldsymbol{L}_{\boldsymbol{d}}^{\mathrm{e}}\boldsymbol{y}^n + \boldsymbol{L}_{\boldsymbol{d}}^{\mathrm{v}}\dot{\boldsymbol{y}}^n - p^n\boldsymbol{n}\|_\Sigma^2 + \frac{\tau}{2\rho^{\mathrm{s}}\epsilon}\|\boldsymbol{L}_{\boldsymbol{d}}^{\mathrm{e}}\boldsymbol{y}^n + \boldsymbol{L}_{\boldsymbol{d}}^{\mathrm{v}}\dot{\boldsymbol{y}}^n\|_\Sigma^2.$$

Therefore,

$$\sum_{i=1}^{4} T_i \geq -\frac{\rho^{\mathrm{s}}\epsilon}{2\tau}\|\dot{\boldsymbol{d}}^n - \dot{\boldsymbol{d}}^{n-1}\|_\Sigma^2 + \frac{\tau}{2\rho^{\mathrm{s}}\epsilon}\|p^n\|_\Sigma^2 + \frac{\tau}{2\rho^{\mathrm{s}}\epsilon}\|\boldsymbol{L}_{\boldsymbol{d}}^{\mathrm{e}}\boldsymbol{y}^n + \boldsymbol{L}_{\boldsymbol{d}}^{\mathrm{v}}\dot{\boldsymbol{y}}^n\|_\Sigma^2. \tag{27}$$

The estimate (19) then follows by inserting this expression into (26), multiplication by τ and summation over $m = 1, ..., n$.

Case $r = 1$. From $(18)_2$, we have

$$\begin{aligned}
T_2 &= \tau^2\left(\partial_\tau\dot{\boldsymbol{d}}^n, \boldsymbol{L}_{\boldsymbol{d}}^{\mathrm{e}}\dot{\boldsymbol{y}}^n + \boldsymbol{L}_{\boldsymbol{d}}^{\mathrm{v}}(\partial_\tau\dot{\boldsymbol{y}}^n)\right)_\Sigma + \tau^2\left(\partial_\tau\dot{\boldsymbol{\theta}}^n, \boldsymbol{L}_{\boldsymbol{\theta}}^{\mathrm{e}}\dot{\boldsymbol{y}}^n + \boldsymbol{L}_{\boldsymbol{\theta}}^{\mathrm{v}}(\partial_\tau\dot{\boldsymbol{y}}^n)\right)_\Sigma \\
&= \tau^2\left(\boldsymbol{Q}^{\mathrm{e}}\dot{\boldsymbol{y}}^n, \partial_\tau\dot{\boldsymbol{y}}^n\right)_\Sigma + \tau^2\left(\boldsymbol{Q}^{\mathrm{v}}\partial_\tau\dot{\boldsymbol{y}}^n, \partial_\tau\dot{\boldsymbol{y}}^n\right)_\Sigma \\
&= \frac{\tau}{2}\left(\|\dot{\boldsymbol{y}}^n\|_{\mathrm{e}}^2 - \left\|\dot{\boldsymbol{y}}^{n-1}\right\|_{\mathrm{e}}^2 + \left\|\dot{\boldsymbol{y}}^n - \dot{\boldsymbol{y}}^{n-1}\right\|_{\mathrm{e}}^2\right) + \tau^2\left\|\partial_\tau\dot{\boldsymbol{y}}^n\right\|_{\mathrm{v}}^2
\end{aligned}$$

for $n \geq 2$. For the third term, we get

$$T_3 \geq -\frac{\rho^{\mathrm{s}}\epsilon}{2\tau}\|\dot{\boldsymbol{d}}^n - \dot{\boldsymbol{d}}^{n-1}\|_\Sigma^2 - \frac{\tau}{2\rho^{\mathrm{s}}\epsilon}\|\left(\boldsymbol{L}_{\boldsymbol{d}}^{\mathrm{e}}\boldsymbol{y}^{n-1}\right)_\perp + \left(\boldsymbol{L}_{\boldsymbol{d}}^{\mathrm{v}}\dot{\boldsymbol{y}}^{n-1}\right)_\perp - p^n\boldsymbol{n}\|_\Sigma^2.$$

At last, the fourth term is estimated as follows

$$\begin{aligned}
T_4 &= \frac{\tau}{\rho^{\mathrm{s}}\epsilon}\left(p^n\boldsymbol{n} - \boldsymbol{L}_{\boldsymbol{d}}^{\mathrm{e}}\boldsymbol{y}^n - \boldsymbol{L}_{\boldsymbol{d}}^{\mathrm{v}}\dot{\boldsymbol{y}}^n, p^n\boldsymbol{n} - \left(\boldsymbol{L}_{\boldsymbol{d}}^{\mathrm{e}}\boldsymbol{y}^{n-1}\right)_\perp - \left(\boldsymbol{L}_{\boldsymbol{d}}^{\mathrm{v}}\dot{\boldsymbol{y}}^{n-1}\right)_\perp\right)_\Sigma \\
&= \frac{\tau}{\rho^{\mathrm{s}}\epsilon}\left(p^n\boldsymbol{n} - \left(\boldsymbol{L}_{\boldsymbol{d}}^{\mathrm{e}}\boldsymbol{y}^n\right)_\perp - \left(\boldsymbol{L}_{\boldsymbol{d}}^{\mathrm{v}}\dot{\boldsymbol{y}}^n\right)_\perp, p^n\boldsymbol{n} - \left(\boldsymbol{L}_{\boldsymbol{d}}^{\mathrm{e}}\boldsymbol{y}^{n-1}\right)_\perp - \left(\boldsymbol{L}_{\boldsymbol{d}}^{\mathrm{v}}\dot{\boldsymbol{y}}^{n-1}\right)_\perp\right)_\Sigma \\
&= \frac{\tau}{\rho^{\mathrm{s}}\epsilon}\|p^n\boldsymbol{n} - \left(\boldsymbol{L}_{\boldsymbol{d}}^{\mathrm{e}}\boldsymbol{y}^{n-1}\right)_\perp - \left(\boldsymbol{L}_{\boldsymbol{d}}^{\mathrm{v}}\dot{\boldsymbol{y}}^{n-1}\right)_\perp\|_\Sigma^2 \\
&\quad - \frac{\tau}{\rho^{\mathrm{s}}\epsilon}\left(\left(\boldsymbol{L}_{\boldsymbol{d}}^{\mathrm{e}}(\boldsymbol{y}^n - \boldsymbol{y}^{n-1})\right)_\perp + \left(\boldsymbol{L}_{\boldsymbol{d}}^{\mathrm{v}}(\dot{\boldsymbol{y}}^n - \dot{\boldsymbol{y}}^{n-1})\right)_\perp, p^n\boldsymbol{n} - \left(\boldsymbol{L}_{\boldsymbol{d}}^{\mathrm{e}}\boldsymbol{y}^{n-1}\right)_\perp - \left(\boldsymbol{L}_{\boldsymbol{d}}^{\mathrm{v}}\dot{\boldsymbol{y}}^{n-1}\right)_\perp\right)_\Sigma \\
&\geq \frac{\tau}{2\rho^{\mathrm{s}}\epsilon}\|p^n\boldsymbol{n} - \left(\boldsymbol{L}_{\boldsymbol{d}}^{\mathrm{e}}\boldsymbol{y}^{n-1}\right)_\perp - \left(\boldsymbol{L}_{\boldsymbol{d}}^{\mathrm{v}}\dot{\boldsymbol{y}}^{n-1}\right)_\perp\|_\Sigma^2 \\
&\quad - \frac{\tau}{2\rho^{\mathrm{s}}\epsilon}\|\left(\boldsymbol{L}_{\boldsymbol{d}}^{\mathrm{e}}(\boldsymbol{y}^n - \boldsymbol{y}^{n-1})\right)_\perp + \left(\boldsymbol{L}_{\boldsymbol{d}}^{\mathrm{v}}(\dot{\boldsymbol{y}}^n - \dot{\boldsymbol{y}}^{n-1})\right)_\perp\|_\Sigma^2.
\end{aligned}$$

Therefore, by collecting the above estimations, we get

$$\begin{aligned}
\sum_{i=1}^{4} T_i \geq &-\frac{\rho^{\mathrm{s}}\epsilon}{2\tau}\|\dot{\boldsymbol{d}}^n - \dot{\boldsymbol{d}}^{n-1}\|_\Sigma^2 + \frac{\tau}{2}\left(\|\dot{\boldsymbol{y}}^n\|_{\mathrm{e}}^2 - \left\|\dot{\boldsymbol{y}}^{n-1}\right\|_{\mathrm{e}}^2 + \left\|\dot{\boldsymbol{y}}^n - \dot{\boldsymbol{y}}^{n-1}\right\|_{\mathrm{e}}^2\right) \\
&+ \tau^2\left\|\partial_\tau\dot{\boldsymbol{y}}^n\right\|_{\mathrm{v}}^2 + \frac{\tau}{2\rho^{\mathrm{s}}\epsilon}\left(\|\boldsymbol{L}_{\boldsymbol{d}}^{\mathrm{e}}\boldsymbol{y}^n + \boldsymbol{L}_{\boldsymbol{d}}^{\mathrm{v}}\dot{\boldsymbol{y}}^n\|_\Sigma^2 - \|\boldsymbol{L}_{\boldsymbol{d}}^{\mathrm{e}}\boldsymbol{y}^{n-1} + \boldsymbol{L}_{\boldsymbol{d}}^{\mathrm{v}}\dot{\boldsymbol{y}}^{n-1}\|_\Sigma^2\right) \\
&+ \frac{\tau}{2\rho^{\mathrm{s}}\epsilon}\left\|\left(\boldsymbol{L}_{\boldsymbol{d}}^{\mathrm{e}}(\boldsymbol{y}^n - \boldsymbol{y}^{n-1})\right)_\parallel + \left(\boldsymbol{L}_{\boldsymbol{d}}^{\mathrm{v}}(\dot{\boldsymbol{y}}^n - \dot{\boldsymbol{y}}^{n-1})\right)_\parallel\right\|_\Sigma^2.
\end{aligned}$$

Inserting this expression into (26), then multiplying by τ and summing over $m = 2, ..., n$, yields the estimate

$$E^n + \sum_{m=2}^{n} D^m \leq E^1 + \frac{\tau}{2} \left\| \boldsymbol{y}^1 - \boldsymbol{y}^0 \right\|_{\mathrm{e}}^2 + \frac{\tau^2}{2\rho^{\mathrm{s}}\epsilon} \| \boldsymbol{L}_{\boldsymbol{d}}^{\mathrm{e}} \boldsymbol{y}^1 + \boldsymbol{L}_{\boldsymbol{d}}^{\mathrm{v}} \dot{\boldsymbol{y}}^1 \|_{\Sigma}^2. \tag{28}$$

Owing to the initialization procedure, $\boldsymbol{y}^1$ and $\dot{\boldsymbol{y}}^1$ are generated from the scheme with $r = 0$. Hence, the right-hand side of (28) can be bounded from (19), with $r = 0$, and the numerical dissipation provided by (25) and (27) for $n = 1$. This completes the proof. □

Remark 3 *The stability of the scheme with the second-order extrapolation $r = 2$ is not covered by the previous analysis. In fact, numerical evidence (not reported here) indicates that this scheme is stable under CFL-like conditions, which can not be derived within a time semi-discrete setting.*

5 Numerical experiments

In this section we illustrate the accuracy and performance of the proposed fully decoupled schemes in several numerical examples from the literature. Section 5.1 focuses on the linear model problem (7)-(8) in a simple two-dimensional geometry. Results based on the nonlinear case (1)-(2) and more complex geometries are presented in the succeeding Sections 5.2-5.4.

5.1 Convergence study in a two-dimensional test-case

The first example simulates a pressure-wave propagation within a compliant channel in 2D. Basically, we couple the Stokes system (7) with a damped generalized string model, i.e., in (8) we take

$$\boldsymbol{d} = \begin{pmatrix} 0 \\ \boldsymbol{d}_y \end{pmatrix}, \quad \boldsymbol{L}^{\mathrm{e}} \boldsymbol{d} = \begin{pmatrix} 0 \\ -\lambda_1 \partial_{xx} \boldsymbol{d}_y + \lambda_0 \boldsymbol{d}_y \end{pmatrix}, \quad \boldsymbol{L}^{\mathrm{v}} \dot{\boldsymbol{d}} = \begin{pmatrix} 0 \\ \alpha \rho^{\mathrm{s}} \epsilon \dot{\boldsymbol{d}}_y - \beta \lambda_1 \partial_{xx} \dot{\boldsymbol{d}}_y \end{pmatrix},$$

with

$$\lambda_1 \overset{\text{def}}{=} \frac{E\epsilon}{2(1+\nu)}, \quad \lambda_0 \overset{\text{def}}{=} \frac{E\epsilon}{R^2(1-\nu^2)},$$

where E denotes the Young modulus and ν the Poisson ratio of the solid. Note that in this case the tangential contributions in $(16)_3$ disappear. The fluid physical parameters are given by $\rho^{\mathrm{f}} = 1.0$ and $\mu = 0.035$, while for the solid we have $\rho^{\mathrm{s}} = 1.1$, $\epsilon = 0.1$, $E = 0.75 \times 10^6$, $\nu = 0.5$, $\alpha = 1$ and $\beta = 10^{-3}$. All units are given in the CGS system. The fluid domain is given by $\Omega = [0, L] \times [0, R]$ and the fluid-solid interface by $\Sigma = [0, L] \times \{R\}$ with $L = 6$ and $R = 0.5$. The overall system is initially at rest and during $5 \cdot 10^{-3}$ seconds, corresponding to half a period, a sinusoidal normal traction of maximal amplitude $2 \cdot 10^4$ is imposed on the inlet boundary $x = 0$. Zero traction is enforced at $x = 6$ and a symmetry condition is applied on the lower wall $y = 0$. The solid is clamped at its extremities, $\boldsymbol{d}_y = 0$ at $x = 0, L$.

Piece-wise affine continuous finite elements are used for the discretization in space of both the fluid and the structure. The numerical computations have been carried out with FreeFem++ [25]. In Figure 2 we report a few snapshots of the pressure field and the solid displacement obtained with Algorithm 2, $r = 1$, $\tau = 10^{-4}$ and $h = 0.05$. The scheme is able to reproduce a stable pressure-wave propagation.

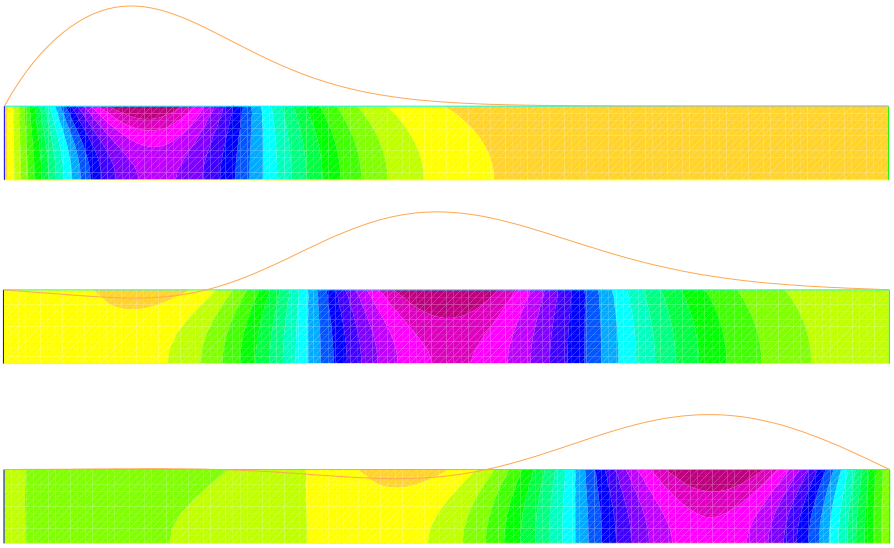

Figure 2: Snapshots of the fluid pressure and solid displacement at $t = 0.005$, 0.01, 0.015 (from top to bottom). Algorithm 2 with first-order extrapolation, $\tau = 10^{-4}$ and $h = 0.05$.

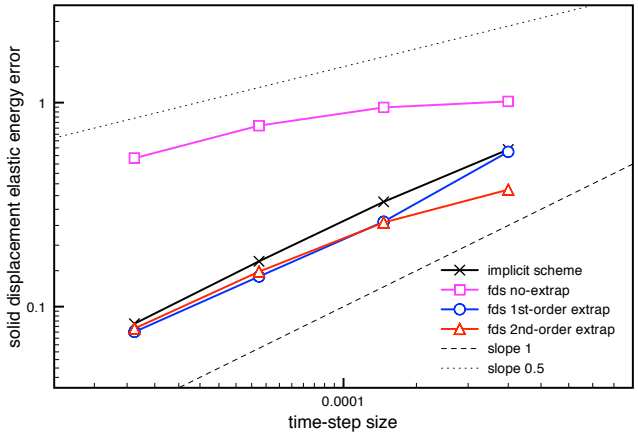

Figure 3: Time-convergence history of the displacement at $t = 0.015$, with $h = \mathcal{O}(\tau)$.

In order to investigate the convergence rate of Algorithm 2, we have uniformly refined both in time and in space according to

$$(\tau, h) = \{5 \cdot 10^{-4}/2^i, 10^{-1}/2^i\}_{i=1}^{4}. \tag{29}$$

Figure 3 reports the time-convergence history of the solid displacement at time $t = 0.015$, in the relative elastic energy-norm, obtained with Algorithm 2 and the different extrapolations ($r = 0, 1, 2$). For comparison purposes the results obtained with a fully implicit first-order scheme are also displayed. The reference solution has been generated using the implicit scheme with a high space-time resolution, $h = 3.125 \times 10^{-3}$ and $\tau = 10^{-6}$. In Figure 4 we aim to complement

the information by showing the actual displacements obtained with the aforementioned schemes at $t = 0.015$. Note that the reference solution is also provided.

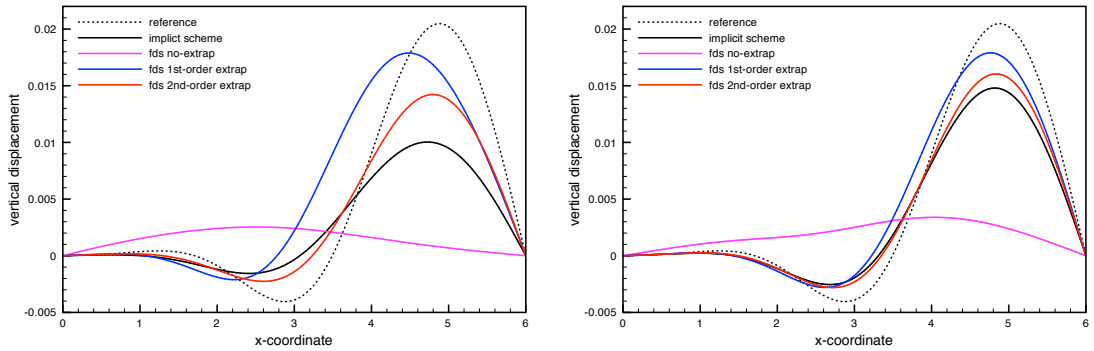

(a) $i = 1$.

(b) $i = 2$.

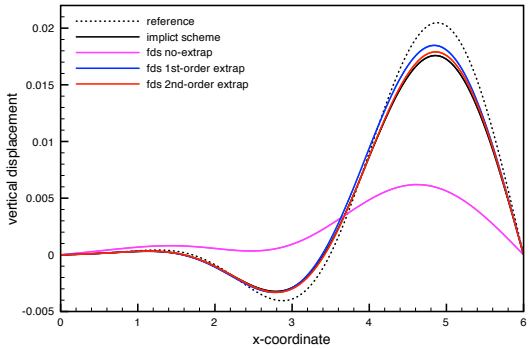

(c) $i = 3$.

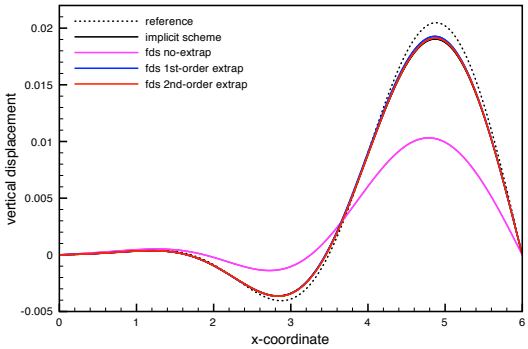

(d) $i = 4$.

Figure 4: Comparison of the solid displacements at $t = 0.015$ for different levels of (τ, h)-refinement, given by (29).

The results show that the proposed fully decoupled scheme with the first- and second-order extrapolations ($r = 1, 2$) are able to retrieve the optimal first-order convergence rate $\mathcal{O}(\tau)$ of the implicit scheme. On the contrary, a sub-optimal overall rate $\mathcal{O}(\tau^{\frac{1}{2}})$ is obtained without extrapolation ($r = 0$).

5.2 Pressure wave propagation in a straight tube

The physical system is described by the non-linear coupled problem (1)-(2), with a Saint Venant-Kirchhoff constitutive law for the solid. The fluid domain is a straight tube of radius $R = 0.5$ and of length $L = 5$. The fluid physical parameters are given by $\rho^{\mathrm{f}} = 1.0$ and $\mu = 0.035$, while for the solid we have $\rho^{\mathrm{s}} = 1.2$, $\epsilon = 0.1$, $E = 3 \times 10^6$ and $\nu = 0.5$. All the units are given in the CGS system. We will consider the case of both a Rayleigh solid damping (see Remark 1) with $\alpha = 1$, $\beta = 10^{-3}$, and an undamped solid ($\alpha = \beta = 0$). The overall system is initially at rest and during $5 \cdot 10^{-3}$ seconds an over pressure of 1.3332×10^4 is imposed on the inlet boundary. Zero traction is enforced at the outlet boundary.

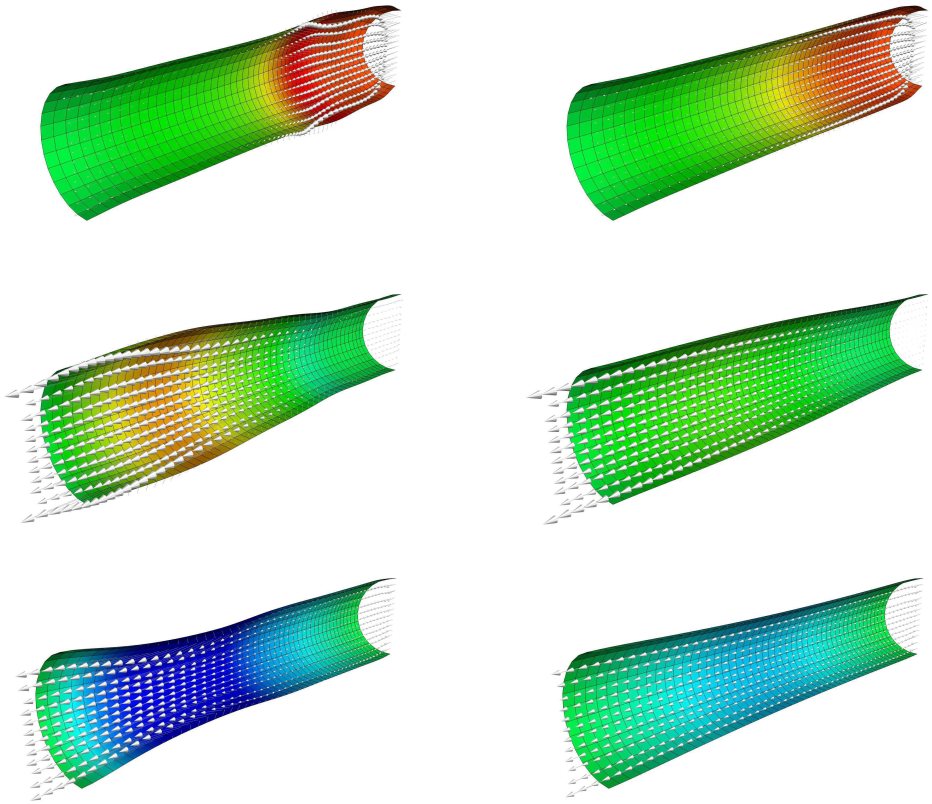

Figure 5: Snapshots of the velocity and fluid interface pressure at $t = 0.005, 0.01, 0.015$ (from top to bottom). Algorithm 1 with first-order extrapolation, $\tau = 10^{-4}$. Left: Shell model without damping ($\alpha = \beta = 0$). Right: Shell model with damping ($\alpha = 1$, $\beta = 10^{-3}$).

Both the velocity and the pressure are discretized in space using $\mathbb{Q}_1$ finite elements. A SUPG stabilization is applied to the viscous sub-step (4) of Algorithm 1. The structure equation is discretized in space by quadrilateral MITC4 shell elements (see [8, Section 8.2.1]).

Figure 5 shows the fluid pressure and the solid deformation (amplified by a factor 10) at different time instants obtained with Algorithm 1 and $r = 1$, in the undamped (left) and damped (right) cases. Here $\tau = 10^{-4}$. A propagating pressure-wave is observed in both situations, being clearly deflated when damping effects are present in the solid model.

For comparison purposes, in Figure 6 we have reported the interface mid-point displacement magnitudes obtained with the three variants of Algorithms 1 and the first-order implicit scheme. The fully decoupled schemes with extrapolation ($r = 1, 2$) are able to retrieve the accuracy of the implicit scheme while the scheme with $r = 0$ provides a very poor approximations. Similar conclusions can be inferred from Figure 7, which reports the out-flows obtained with the different schemes.

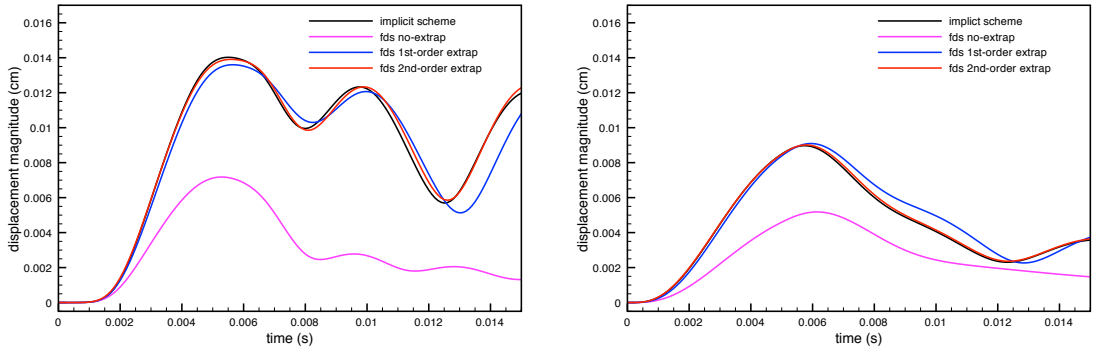

Figure 6: Comparison of the implicit and fully decoupled schemes: interface mid-point displacement magnitude *vs.* time. Left: Shell model without damping ($\alpha = \beta = 0$). Right: Shell model with damping ($\alpha = 1$, $\beta = 10^{-3}$).

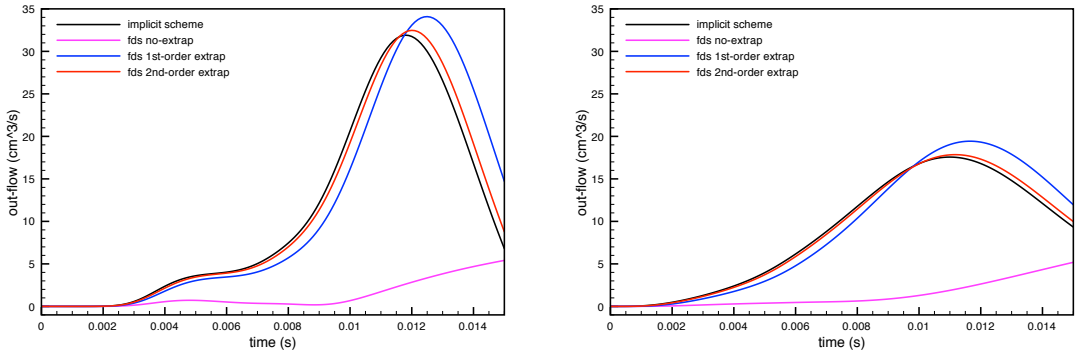

Figure 7: Comparison of the implicit and fully decoupled schemes: out-flow *vs.* time. Left: Shell model without damping ($\alpha = \beta = 0$). Right: Shell model with damping ($\alpha = 1$, $\beta = 10^{-3}$).

5.3 Blood flow in an abdominal aortic aneurysm

The fluid computational domain is the idealized abdominal aortic aneurysm (we refer to [35] for the details). The whole compliant wall has a uniform thickness of 0.17 and length of 22.95. All units are given in the CGS system. The fluid physical parameters are given by $\rho^{\mathrm{f}} = 1.0$ and $\mu = 0.035$ while for the solid we have $\rho^{\mathrm{s}} = 1.2$, $\epsilon = 0.17$, $E = 3 \times 10^6$, $\nu = 0.5$, $\alpha = 1$ and $\beta = 10^{-3}$. Initially, the fluid is at rest. On the inlet boundary, we impose a flow rate waveform obtained form measurements at the level of the infrarenal aorta (see Figure 8). A resistive-like boundary condition is prescribed on the outlet boundary, the value of the resistance being $R_{\mathrm{out}} = 600$.

We consider Algorithm 1 with the same spatial discretization than in the previous example. We have simulated 2000 time steps of size $\tau = 4.2 \times 10^{-4}$ s, which corresponds to a complete cardiac cycle. For illustration purpose, we have reported in Figure 8 the resulting velocity magnitude distribution for different time instants obtained with Algorithm 1 and $r = 1$. Figure 9 displays the interface midpoint displacement magnitudes and outflows obtained with Algorithm 1 and the first-order implicit coupling scheme. The impact of the extrapolations on the accuracy of

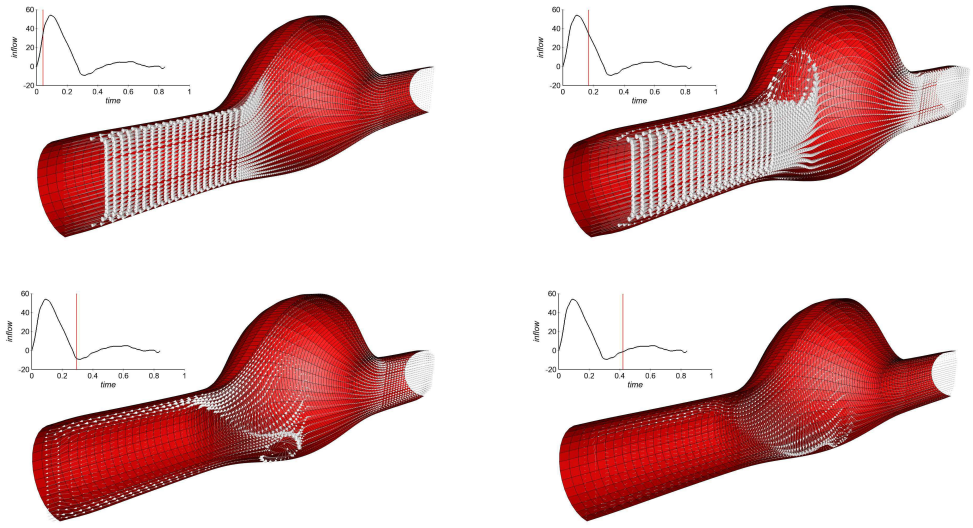

Figure 8: Snapshots of the fluid velocity $t = 0.042, 0.168, 0.294, 0.42$ (from left to right and top to bottom). Algorithm 1 with first-order extrapolation, $\tau = 4.2 \cdot 10^{-4}$.

Algorithm 1 is clearly visible. Without extrapolation ($r = 0$), the fully decoupled scheme yields a extremely poor approximation. The variant with the first- and second-order extrapolations ($r = 1, 2$) provide numerical solutions close to the implicit coupling scheme. The superior accuracy of the second-order extrapolation is striking.

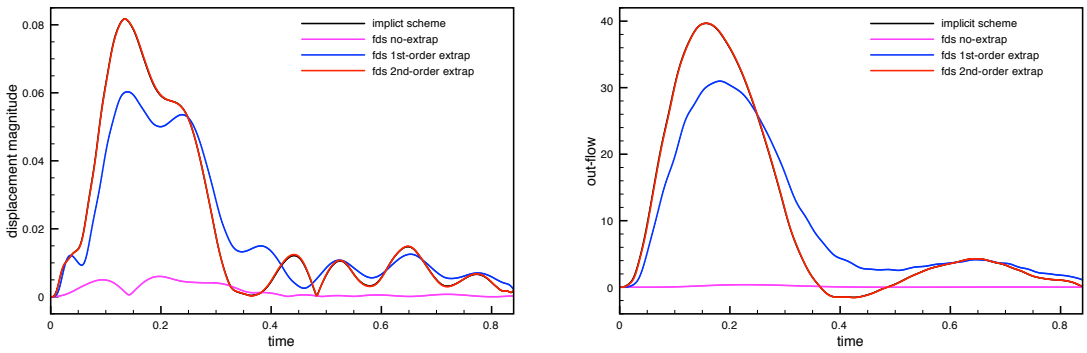

Figure 9: Comparison of the implicit and fully decoupled schemes: Left: Interface displacement. Right: Out-flow.

5.4 Damped structural instability

We consider a bended fluid domain surrounded by two thin structures with different stiffness, as proposed in [28]. The physical system is described by the non-linear coupled problem (1)-(2), with a Saint Venant-Kirchhoff constitutive law for the solid. The fluid physical parameters are

in this case given by by $\rho^{\mathrm{f}} = 1.0$ and $\mu = 9$, while for the top and bottom (undamped) structures we have $\rho^{\mathrm{s}} = 500$, $\epsilon = 0.1$, $E_{\mathrm{top}} = 9 \cdot 10^5$, $E_{\mathrm{bottom}} = 9 \cdot 10^8$ and $\nu = 0.3$. All the units are given in the SI system. A constant parabolic velocity profile is prescribed on the left and right inflow boundaries, with maximal magnitudes 10 and 10.1, respectively (to avoid perfect symmetry). Zero velocity is enforced on the remaining fluid boundaries. The fluid is loaded with the volume force $\boldsymbol{f} = (0, -1)^{\mathrm{T}}$.

We consider Algorithm 1 with the same spatial discretization than in the previous example. The simulations are performed in three-dimensions by imposing symmetry conditions along the extrusion direction.

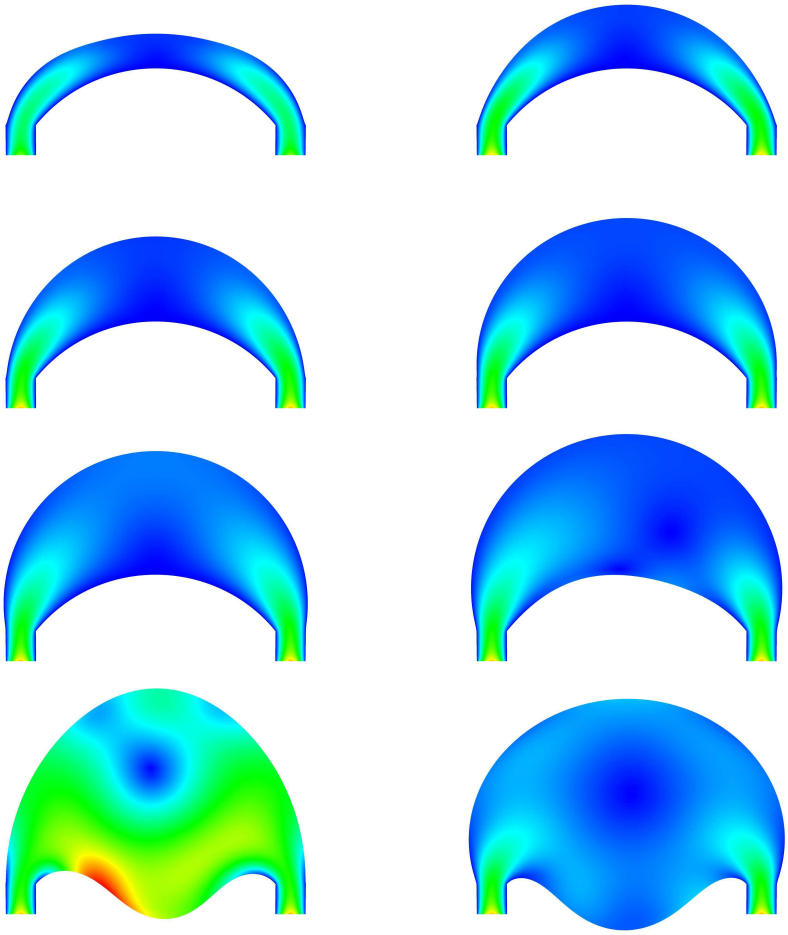

Figure 10: Snapshots of the fluid velocity $t = 0.5$, 1, 1.5, 2, 2.5, 3, 3.5, 4 (from left to right and top to bottom). Algorithm 1 with first-order extrapolation.

In Figure 10 we have reported the fluid velocity magnitude snapshots and the solid deformations at different time instants, obtained with Algorithm 1 (first-order extrapolation) and time-step length of $\tau = 0.005$. As in [28], the deformation is first mainly visible in the upper (more flexible) structure and then, when the fluid pressure reaches a critical value, the lower

structure buckles.

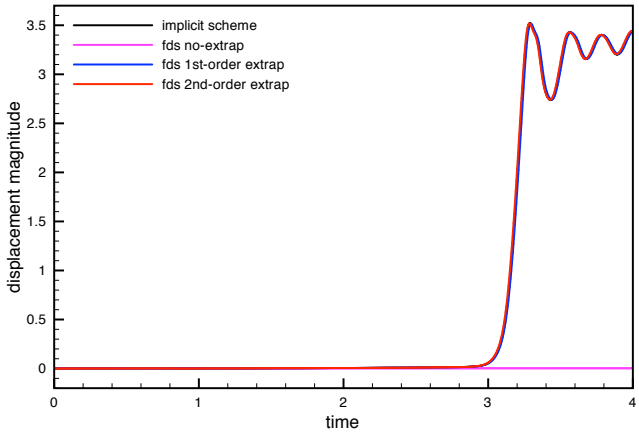

Figure 11: Comparison of the implicit and fully decoupled schemes: interface mid-point displacement magnitude of the bottom structure *vs.* time.

Figure 11 reports the interface mid-point displacement magnitude of the bottom structure obtained with Algorithm 1 and the different extrapolations. The poor accuracy of the scheme without extrapolation is striking: the lower order perturbation of the kinematic coupling yields an excess of mass-loss across the interface which prevents the buckling. On the contrary, the variants with the first- and second-order extrapolations give practically the same result and accurately predict the collapse of the bottom structure.

6 Conclusion

In this work we have introduced a new class of coupling schemes for fluid-structure interaction problems involving an incompressible fluid and a general thin-walled viscoelastic structure (Reissner-Mindlin shell). The methods proposed allow a fully decoupled time-marching of the complete fluid-solid state: fluid velocity, fluid pressure and solid displacement. The basic ingredients of this fluid-solid splitting paradigm are:

- fractional-step time-marching in the fluid (Chorin-Temam scheme);
- appropriate fractional-step time-marching of the interface Robin consistency (9), which yields explicit interface Robin conditions for the fluid sub-steps (only inertial effects are treated implicitly);
- fluid stresses are transferred to the thin-walled structure in a standard fashion.

Unconditional stability has been proved for the variants with zeroth- and first-order extrapolation ($r = 0, 1$) in a representative liner setting (Theorem 1). Though not covered by the stability analysis, numerical evidence has shown that the second-order extrapolation is stable for a reasonable range of the discretization parameters. The comprehensive numerical study indicates also that the best accuracy and robustness is obtained with the first- and second-order extrapolated variants ($r = 1, 2$). In particular, they retrieve the overall first-order accuracy of the fully implicit scheme.

Further extensions of this work can explore various directions. We can consider the extension to second-order time-marching schemes (e.g., via incremental pressure-correction in the fluid and overall second-order time-stepping), the analysis of the variant with second-order extrapolation and, more generally, the analysis in a fully discrete setting and the derivation of a priori error estimates. Another important setting, not cover by this work, is the case of the coupling with thick-walled structures. In this line, it is worth mentioning that the combination of the ideas reported in [20] with the present coupling paradigm could spoil the first-order overall accuracy. Hence, alternative approaches need to be explored.

Acknowledgements

The authors are thankful to Marina Vidrascu (Inria) for her support on the non-linear shell solver.

References

[1] M. Astorino, F. Chouly, and M. A. Fernández. Robin based semi-implicit coupling in fluid-structure interaction: Stability analysis and numerics. *SIAM J. Sci. Comput.*, 31(6):4041–4065, 2009.

[2] M. Astorino and C. Grandmont. Convergence analysis of a projection semi-implicit coupling scheme for fluid-structure interaction problems. *Numer. Math.*, 116:721–767, 2010.

[3] S. Badia, A. Quaini, and A. Quarteroni. Splitting methods based on algebraic factorization for fluid-structure interaction. *SIAM J. Sci. Comput.*, 30(4):1778–1805, 2008.

[4] M. Bischoff, K.-U. Bletzinger, W.A. Wall, and E. Ramm. *Models and Finite Elements for Thin-Walled Structures*, chapter 3. John Wiley & Sons, Ltd, 2004.

[5] M. Bukac, C. Canic, R. Glowinski, T. Tambaca, and A. Quaini. Fluid-structure interaction in blood flow capturing non-zero longitudinal structure displacement. *J. Comp. Phys.*, 235(0):515–541, 2013.

[6] S. Čanić, J. Tambača, G. Guidoboni, A. Mikelić, C.J. Hartley, and D. Rosenstrauch. Modeling viscoelastic behavior of arterial walls and their interaction with pulsatile blood flow. *SIAM J. Appl. Math.*, 67(1):164–193, 2006.

[7] P. Causin, J.-F. Gerbeau, and F. Nobile. Added-mass effect in the design of partitioned algorithms for fluid-structure problems. *Comput. Methods Appl. Mech. Engrg.*, 194(42–44):4506–4527, 2005.

[8] D. Chapelle and K.J. Bathe. *The Finite Element Analysis of Shells - Fundamentals*. Springer, 2011.

[9] A.J. Chorin. Numerical solution of the Navier-Stokes equations. *Math. Comp.*, 22:745–762, 1968.

[10] J. Donéa, S. Giuliani, and J. P. Halleux. An arbitrary Lagrangian-Eulerian finite element method for transient dynamic fluid-structure interactions. *Comp. Meth. Appl. Mech. Engng.*, pages 689–723, 1982.

[11] M. Eswaran, U.K. Saha, and D. Maity. Effect of baffles on a partially filled cubic tank: Numerical simulation and experimental validation. *Computers & Structures*, 87(3–4):198–205, 2009.

[12] M.A. Fernández. Coupling schemes for incompressible fluid-structure interaction: implicit, semi-implicit and explicit. *SEMA J.*, 55(1):59–108, 2011.

[13] M.A. Fernández. Incremental displacement-correction schemes for the explicit coupling of a thin structure with an incompressible fluid. *C. R. Math. Acad. Sci. Paris*, 349(7-8):473–477, 2011.

[14] M.A. Fernández. Incremental displacement-correction schemes for incompressible fluid-structure interaction: stability and convergence analysis. *Numer. Math.*, 123(1):21–65, 2013.

[15] M.A. Fernández, J.-F. Gerbeau, and C. Grandmont. A projection algorithm for fluid-structure interaction problems with strong added-mass effect. *C. R. Math. Acad. Sci. Paris*, 342(4):279–284, 2006.

[16] M.A. Fernández, J.F. Gerbeau, and C. Grandmont. A projection semi-implicit scheme for the coupling of an elastic structure with an incompressible fluid. *Int. J. Num. Meth. Engrg.*, 69(4):794–821, 2007.

[17] M.A. Fernández and M. Landajuela. A fully decoupled scheme for the interaction of a thin-walled structure with an incompressible fluid. *C. R. Math. Acad. Sci. Paris*, 351(3-4):161–164, 2013.

[18] M.A. Fernández and J. Mullaert. Displacement-velocity correction schemes for incompressible fluid-structure interaction. *C. R. Math. Acad. Sci. Paris*, 349(17-18):1011–1015, 2011.

[19] M.A. Fernández, J. Mullaert, and M. Vidrascu. Explicit Robin-Neumann schemes for the coupling of incompressible fluids with thin-walled structures. *Comput. Methods Appl. Mech. Engrg.*, 267:566–593, 2013.

[20] M.A. Fernández, J. Mullaert, and M. Vidrascu. Generalized Robin-Neumann explicit coupling schemes for incompressible fluid-structure interaction: stability analysis and numerics. Research Report RR-8384, INRIA, 2013.

[21] L. Formaggia, A. Quarteroni, and A. Veneziani, editors. *Cardiovascular Mathematics. Modeling and simulation of the circulatory system*, volume 1 of *Modeling, Simulation and Applications*. Springer, 2009.

[22] J.-L. Guermond. Some implementation of projection methods for Navier-Stokes equations. *M2AN Math. Model. Numer. Anal.*, 30:637–667, 1996.

[23] J. L. Guermond, P. Minev, and J. Shen. An overview of projection methods for incompressible flows. *Comput. Methods Appl. Mech. Engrg.*, 195(44-47):6011–6045, 2006.

[24] G. Guidoboni, R. Glowinski, N. Cavallini, and S. Canic. Stable loosely-coupled-type algorithm for fluid-structure interaction in blood flow. *J. Comp. Phys.*, 228(18):6916–6937, 2009.

[25] F. Hecht. New development in FreeFem++. *J. Numer. Math.*, 20(3-4):251–265, 2012.

[26] M. Heil and A.L. Hazel. Fluid-structure interaction in internal physiological flows. In *Annual review of fluid mechanics. Volume 43, 2011*, volume 43 of *Annu. Rev. Fluid Mech.*, pages 141–162. Annual Reviews, 2011.

[27] P. Kalita and R. Schaefer. Mechanical models of artery walls. *Arch. Comput. Methods Eng.*, 15(1):1–36, 2008.

[28] U. Küttler, C. Förster, and W.A. Wall. A solution for the incompressibility dilemma in partitioned fluid–structure interaction with pure Dirichlet fluid domains. *Comput. Mech.*, 38:417–429, 2006.

[29] M. Lombardi, N. Parolini, A. Quarteroni, and G. Rozza. Numerical simulation of sailing boats: Dynamics, FSI, and shape optimization. In G. Buttazzo and A. Frediani, editors, *Variational Analysis and Aerospace Engineering: Mathematical Challenges for Aerospace Design*, Springer Optimization and Its Applications, pages 339–377. Springer, 2012.

[30] M. Lukacova-Medvid'ovaa, G. Rusnakovaa, and A. Hundertmark-Zauskovaa. Kinematic splitting algorithm for fluid-structure interaction in hemodynamics. *Comput. Methods Appl. Mech. Engrg.*, 265(1):83–106, 2013.

[31] P. Moireau, N. Xiao, M. Astorino, C. A. Figueroa, D. Chapelle, C. A. Taylor, and J-F. Gerbeau. External tissue support and fluid-structure simulation in blood flows. *Biomech. Model. Mechanobiol.*, 11:1–18, 2012.

[32] F. Nobile and C. Vergara. An effective fluid-structure interaction formulation for vascular dynamics by generalized Robin conditions. *SIAM J. Sci. Comput.*, 30(2):731–763, 2008.

[33] M.P. Païdoussis, S.J. Price, and E. de Langre. *Fluid-structure interactions: cross-flow-induced instabilities*. Cambridge University Press, 2011.

[34] A. Quaini and A. Quarteroni. A semi-implicit approach for fluid-structure interaction based on an algebraic fractional step method. *Math. Models Methods Appl. Sci.*, 17(6):957–983, 2007.

[35] A.-V. Salsac, S.R. Sparks, J.M. Chomaz, and J.C. Lasheras. Evolution of the wall shear stresses during the progressive enlargement of symmetric abdominal aortic aneurysms. *J. Fluid Mech.*, 550:19–51, 2006.

[36] K. Takizawa and T.E. Tezduyar. Computational methods for parachute fluid-structure interactions. *Arch. Comput. Methods Eng.*, 19:125–169, 2012.

[37] R. Temam. Une méthode d'approximation de la solution des équations de Navier-Stokes. *Bull. Soc. Math. France*, 96:115–152, 1968.

[38] D. Valdez-Jasso, H.T. Banks, M.A. Haider, D. Bia, Y. Zocalo, R.L. Armentano, and M.S. Olufsen. Viscoelastic models for passive arterial wall dynamics. *Adv. Appl. Math. Mech.*, 1(2):151–165, 2009.

Contents

1 Introduction **3**

2 Problem setting **4**

3 A class of fully decoupled schemes **5**

4 Derivation and analysis in the linear case **5**
4.1 Time semi-discretization 7
4.2 Stability analysis 8
4.2.1 Preliminaries 9
4.2.2 A priori energy estimate 10

5 Numerical experiments **13**
5.1 Convergence study in a two-dimensional test-case 13
5.2 Pressure wave propagation in a straight tube 15
5.3 Blood flow in an abdominal aortic aneurysm 17
5.4 Damped structural instability 18

6 Conclusion **20**

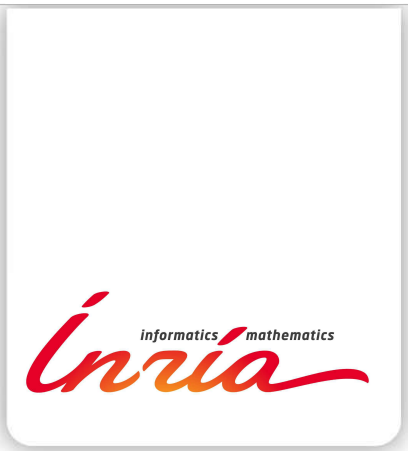

RESEARCH CENTRE
PARIS – ROCQUENCOURT

Domaine de Voluceau, - Rocquencourt
B.P. 105 - 78153 Le Chesnay Cedex

Publisher
Inria
Domaine de Voluceau - Rocquencourt
BP 105 - 78153 Le Chesnay Cedex
inria.fr

ISSN 0249-6399